



INSTITUT FÜR
ENERGIETECHNIK
UND THERMODYNAMIK
Institute of Energy Systems and Thermodynamics



MEDIZINISCHE
UNIVERSITÄT WIEN

Master's Thesis

Dynamic Behaviour due to Pulsatile Boundary Conditions in Rotodynamic Blood Pumps

under the supervision of

Assistant Prof. Dipl.-Ing. Semlitsch Bernhard, PhD

E302 - Institute of Energy Systems and Thermodynamics

Technische Universität Wien

Associate Prof. Marcus Granegger, PhD

Department of Cardiac Surgery

Medizinische Universität Wien

submitted to the Faculty of Mechanical and Industrial Engineering

of Technische Universität Wien

for the degree of Diplom-Ingenieur (Dipl.-Ing.)

by

Simon Klocker, BSc

Matr.Nr. 01526685



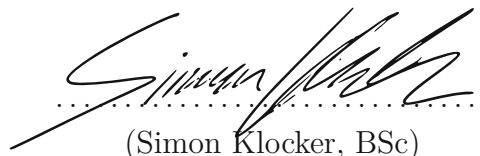
Die approbierte gedruckte Originalversion dieser Diplomarbeit ist an der TU Wien Bibliothek verfügbar
The approved original version of this thesis is available in print at TU Wien Bibliothek.

Statutory Declaration

This thesis is the result of my own work and includes nothing that is the outcome of work done in collaboration except as specified in the text.

It is not substantially the same as any that I have submitted, or, is being concurrently submitted for a degree or diploma or other qualification at Technische Universität Wien or any other University or similar institution except as specified in the text. I further state that no substantial part of my thesis has already been submitted, or, is being concurrently submitted for any such degree, diploma or other qualification at Technische Universität Wien or any other University or similar institution except as specified in the text.

Wien, August 2024



(Simon Klocker, BSc)



Die approbierte gedruckte Originalversion dieser Diplomarbeit ist an der TU Wien Bibliothek verfügbar
The approved original version of this thesis is available in print at TU Wien Bibliothek.

Abstract

Rotodynamic blood pumps (RBPs) provide a therapeutic solution for patients with congestive heart failure who are ineligible for transplantation or require bridging support while awaiting a transplant. While static Computational Fluid Dynamics (CFD) simulations are commonly used to predict flow conditions and ensure the avoidance of blood damage, they do not accurately represent realistic conditions. Since RBPs are directly connected to the cardiovascular interface, they operate in a highly dynamic and transient manner. The aim of this study was to establish a framework for transient CFD simulations to capture the realistic boundary conditions set by the cardiovascular interface. These investigations were carried out for the HeartMate III.

To adequately distinguish the effects of static and transient simulations, various methodologies—such as interface modeling, impeller positioning, turbulence, motion modeling, and surface roughness—were initially investigated in a static context and validated with in-vitro results. Pulsatile boundary conditions representing tandem operation with the native heart were subsequently applied in the CFD simulations. The effects of turbulence, motion modeling, speed fluctuations, and time steps were investigated numerically, while the inlet flow conditions were examined experimentally. The simulation setups were validated with dynamic in-vitro results.

Although the deviation between experimental and numerical results for static operation could not be identified (73.6 *mmHg* vs. 82.7 *mmHg* at 4.5 *l/min* and 5400 *rpm*), questions regarding the interface's position, turbulence modelling and surface roughness could be clarified.

The dynamic behavior resulting from pulsatile boundary conditions can be accurately simulated if static errors are properly accounted for, emphasizing the importance of precise static simulations across the entire flow rate range. Additionally, the methodology combining a *moving reference frame* with a *mixing plane* performed as effectively as the *sliding mesh* approach for time steps up to 36 deg, offering the potential to reduce computational costs.



Die approbierte gedruckte Originalversion dieser Diplomarbeit ist an der TU Wien Bibliothek verfügbar
The approved original version of this thesis is available in print at TU Wien Bibliothek.

Kurzfassung

Rotodynamische Blutpumpen (RBPs) bieten eine therapeutische Lösung für Patienten mit Herzinsuffizienz, die entweder nicht für eine Transplantation in Frage kommen oder eine temporäre Unterstützung während des Wartens auf eine Transplantation benötigen. Statische Computational Fluid Dynamics (CFD)-Simulationen werden häufig verwendet, um Strömungsbedingungen vorherzusagen und sicherzustellen, dass Blutschäden vermieden werden. Diese Simulationen stellen jedoch nicht immer realistische Bedingungen dar. Da RBPs direkt mit dem kardiovaskulären System verbunden sind, arbeiten sie auf stark dynamische und transiente Weise. Ziel dieser Studie war es, einen Standard für transiente CFD-Simulationen zu entwickeln, welcher realistische Randbedingungen berücksichtigt. Die Untersuchungen wurden am HeartMate III durchgeführt.

Um die Auswirkungen statischer und transienter Simulationen angemessen zu unterscheiden, wurden verschiedene Methoden — wie Interface-Positionierung, Impeller-Positionierung, Turbulenzmodellierung, Bewegungsmodellierung und Oberflächenrauigkeit — zunächst im statischen Kontext untersucht und mit in-vitro-Ergebnissen validiert. Anschließend wurden pulsatile Randbedingungen, die den Tandembetrieb mit dem natürlichen Herzen repräsentieren, in die CFD-Simulationen integriert. Die Auswirkungen von Turbulenzmodellierung, Bewegungsmodellierung, Geschwindigkeitsfluktuationen und Zeitschritten wurden numerisch untersucht, während die Einlassströmungsbedingungen experimentell überprüft wurden. Die Simulationen wurden mit dynamischen in-vitro-Ergebnissen validiert.

Obwohl die Abweichungen zwischen experimentellen und numerischen Ergebnissen für den statischen Betrieb (73.6 mmHg vs. 82.7 mmHg bei 4.5 l/min und 5400 rpm) nicht vollständig geklärt werden konnten, konnten Fragen zur Position des Interfaces, zur Turbulenzmodellierung und zur Oberflächenrauigkeit geklärt werden.

Das dynamische Verhalten, das sich aus pulsierenden Randbedingungen ergibt, kann durch Simulation abgebildet werden, wenn statische Fehler angemessen berücksichtigt werden, was die Bedeutung präziser statischer Simulationen über den gesamten Durchflussbereich unterstreicht. Darüber hinaus erwies sich die Methode, Moving Reference Frame in Kombination mit Mixing Plane, für Zeitschritte bis 36° als ebenso effektiv wie der Sliding-Mesh-Ansatz und bietet das Potenzial zur Reduzierung des Rechenaufwands.



Die approbierte gedruckte Originalversion dieser Diplomarbeit ist an der TU Wien Bibliothek verfügbar
The approved original version of this thesis is available in print at TU Wien Bibliothek.

Table of Contents

1 Introduction	1
1.1 History of mechanical circulatory support	1
1.2 Introduction of the investigated LVAD - HeartMate III	4
1.3 Hemodynamics	5
1.3.1 Static characteristics	7
1.3.2 Dynamic characteristics	10
1.4 Hemocompatibility	11
1.5 Principles of computational fluid dynamics	13
1.6 State-of-the-art	19
1.6.1 Static characterisation of rotodynamic blood pumps	19
1.6.2 Dynamic characterisation of rotodynamic blood pumps	21
2 Objective 1 - Static Investigation	24
2.1 Methods	26
2.1.1 Experimental Setup	26
2.1.2 Setup with modified Inlet	26
2.1.3 Numerical Setup	27
2.1.4 Investigation of Interfaces	29
2.1.5 Investigation of the Impeller Position	30
2.1.6 Investigation of Turbulence	30
2.1.7 Investigation of Motion Modelling	31
2.1.8 Investigation of Roughness	31
2.2 Results	33
2.2.1 Experimental Results	33
2.2.2 Investigation of Interfaces	34
2.2.3 Investigation of the Impeller Position	35

2.2.4	Investigation of Turbulence	36
2.2.5	Investigation of Motion Modelling	37
2.2.6	Investigation of Roughness	37
2.2.7	Comparison of the Experimental and Simulated Results	38
2.3	Discussion	39
2.4	Conclusion	42
3	Objective 2 - Dynamic Investigation	44
3.1	Method	44
3.1.1	Experimental Setup	44
3.1.2	Numerical Setup	45
3.2	Results	46
3.2.1	Experimental Results	46
3.2.2	Investigation of Boundary Condition	48
3.2.3	Investigation of Turbulence	48
3.2.4	Investigation of Motion	49
3.2.5	Investigation of Speed Fluctuations	50
3.2.6	Investigation of Time Steps	50
3.2.7	Comparison of Experimental and Numerical Results	51
3.3	Discussion	53
3.3.1	Experimental Results	53
3.3.2	Numerical Results	56
3.3.3	Comparison of Experimental and Numerical Results	57
3.4	Conclusion	57
	Bibliography	59

Nomenclature

Abbreviations

BTR	Bridge-To-Recovery
BTT	Bridge-To-Transplant
CFD	Computational Fluid Dynamics
FDA	Food and Drug Administration
HM3	HeartMate III
LVAD	Left ventricular assist devices

Latin Symbols

A_{eq}	Cross section area of equivalent pipe	m^2
d_1	Diameter at blade channel inlet	m
d_2	Diameter at blade channel outlet	m
$d_{1,eff}$	Effective diameter at blade channel inlet	m
E	Total energy	J
f	Friction factor	
f_r	Roughness function	
g	Gravitational acceleration	m/s^2
H	Head pressure	mmHg
$H()$	Spatial finite-difference operator	
H_{dyn}	Dynamic change in head pressure	mmHg
H_{EUL}	Theoretical head pressure	mmHg
H_{fri}	Friction loss	mmHg
H_{inc}	Incidence loss	mmHg
H_{rec}	Loss due part-load recirculation	mmHg
H_{tot}	Total enthalpy	J
k	Turbulent kinetic energy	
L	Characteristic length	m
L_{eq}	Length of equivalent pipe	m
m	Hydraulic radius	m
n	Rotational speed	rpm
p	Pressure	Pa
P_b	Production due to buoyancy	
P_k	Production due to mean velocity shear	

Nomenclature

Q	Volumetric flow rate	L/min
q_H	External heat	J
Q_{des}	Volumetric flow rate at design point	L/min
q_{inf}	Volumetric flow rate at inflection point	L/min
r	Equivalent sand grain roughness	
R^+	Roughness parameter	
S_i	External source of momentum	kg m/s
$S_{k,\epsilon,\omega}$	User defined source	
T	Temperature	K
t_{exp}	Exposure time	s
u	Velocity	m/s
u^+	Dimensionless velocity	
u_2	Circumferential discharge velocity	m/s
u_{m2}	Meridional discharge velocity	m/s
W_f	Work of external forces	J
y^+	Dimensionless wall distance	

Greek Symbols

β_2	Discharge angle	°
δt	Discretized time	s
Δ_i	Finite-difference equivalent of the gradient	
δ_{ij}	<i>Kronecker delta</i>	
ϵ	Dissipation rate	
κ	<i>Karman constant</i>	
μ	Dynamic viscosity	Pa s
∇	Divergence operator	
ν	Kinematic viscosity	m ² /s
ν_t	Turbulent eddy viscosity	
ω	Specific eddy viscosity	
ρ	Density	kg/m ³
τ	Shear stress	Pa

Vectors and Tensors

$\bar{\bar{\tau}}$	Stress tensor
$\bar{\bar{I}}$	Identity matrix
\mathbf{f}_e	Vector of external forces

Nomenclature

\mathbf{u}	Vector of absolute velocity
τ_{turb}	Reynolds stress tensor

Subscripts

fHb	Free hemoglobin
Hb	Total hemoglobin
HI[%]	Hemolysis index
Re	Reynolds Number
RMSE	Root mean square error



Die approbierte gedruckte Originalversion dieser Diplomarbeit ist an der TU Wien Bibliothek verfügbar
The approved original version of this thesis is available in print at TU Wien Bibliothek.

Chapter 1

Introduction

Congestive heart failure, i.e. a reduced ejection capacity of one or both ventricles, is still a major challenge in health care. First and foremost, the high morbidity and mortality need to be addressed, as well as the significant costs incurred by the healthcare system [9]. In the case of end-stage heart failure, cardiac transplantation often offers the best treatment but is limited by donor organ availability. Figure 1.1 shows the active waiting list for heart donations compared to the deceased donors used annually in the participating countries of Eurotransplant [12].

Left ventricular assist devices (LVAD) can be used to bridge the time to transplantation (BTT), as a temporal solution until cardiac functions recover (BTR) or as a long-term alternative to a donor heart for patients with end-stage heart failure ineligible for transplantation (DT) [39]. The challenge from an engineering perspective is to design a device that provides the necessary hemodynamics while assuring hemocompatibility and avoiding blood damage. The computational fluid dynamics (CFD) method, combined with experimental studies, offers a way to understand complex processes and optimise devices. Therefore, validated simulation setups are required to accurately predict the flow, hemodynamic and blood damage outcomes.

1.1 History of mechanical circulatory support

The idea of a device that would serve as a bridge to transplantation in the event of cardiogenic shock emerged as early as the late 1960s. Back then, the devices were paracorporeal and often used a pneumatic drive, such as the VAD designed by Dr.

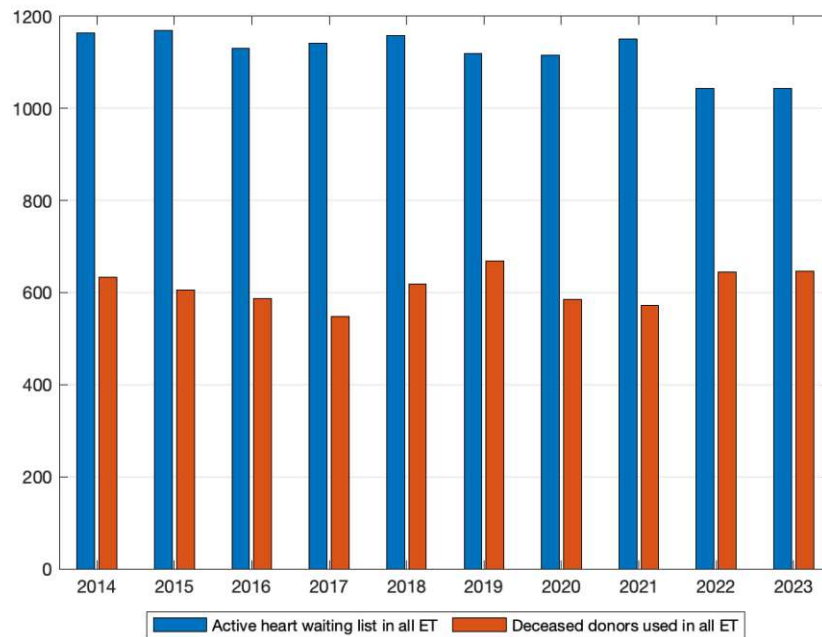


Figure 1.1: Active heart waiting list compared to the deceased donors used in all Eurotransplant participating countries [12].

William Pierce [9]. His device was further developed as the Thoratec VAD and was the first approved by the Food and Drug Administration for postcardiotomy applications and as a BTT application [37]. Over 4000 patients benefited from this device [9].

The first implantable LVAD, Thoratec HeartMate XVE, was approved by the FDA in November 2002 for BTT after a prior study showed that the survival rate increased from 25% (optimal medical therapy) up to 52% after one year and from 8% to 22% after two years [42]. These numbers demonstrate the improvement compared to optimal medical therapy for non-eligible patients for transplants but are significantly worse than for heart transplant recipients. The HeartMate XVE provided a pulsatile flow and was electrically powered [9]. Displacement pumps providing pulsatile flow are considered first-generation LVADs.

With the second generation, the development focused on the rotodynamic pump principle, which delivers a continuous instead of pulsatile flow. Thoratec's successor model, the HeartMate II, is not only designed as an axial pump, it also weighs about 70% less than the HeartMate XVE [49]. With the continuous flow, the survival rate after two years increased to 58% compared to 22% with the previous

pulsatile flow devices. Furthermore, adverse events occurred less often, and pump replacements were less frequent due to higher durability [44]. Consequently, the HeartMate II was approved by the FDA in 2008 [23]. Nevertheless, major challenges are still adverse events, including bleeding, stroke, right heart failure, percutaneous lead infection, and pump thrombosis [9]. After pump thrombosis increased in 2011, multiple causes were investigated in the PREVENT (Prevention of HeartMate II Pump Thrombosis through Clinical Management) trial [28]. Although the trial could not identify the exact cause, one possible cause could be the pivot bearing between the spinning rotor and the stator. In this area, not only is a lot of heat generated by friction, but relative flow stasis occurs, leading to a poor washout at the end of the pump stage [24].

The impeller is suspended in the blood flow using hydrodynamic or magnetic levitation in the third-generation [24] to avoid mechanical contact bearings. Another feature included in most third-generation devices is a speed modulation program with the intention of a higher washout and introducing pulsatility. An early representative of the third generation of LVAD was the HVAD (HeartWare Ventricle Assist Device, Medtronic, Minneapolis, MN, USA), approved by the FDA in 2012. The ENDURANCE trial was the first head-to-head trial between HVAD and HeartMate II. While the trial showed that the HVAD is non-inferior to an axial pump regarding survival rates, the pump replacement decreased, and interestingly, the stroke rate increased dramatically (29.7% vs. 12.1%) [41]. This observation led to a follow-up trial in which blood pressure was identified as a risk factor. With an enhanced blood pressure protocol, the stroke risk with the HVAD was reduced by 25% [33]. In 2018, the HeartMate III (HM3, Abbott, Chicago, IL, USA) was approved by the Food and Drug Administration (FDA), a centrifugal pump with magnetic levitation. The direct comparison with the axial pump HeartMate II showed a higher survival rate after two years (76.9% vs 64.8%), as reported in the MOMENTUM 3 trial [31]. While the centrifugal pump performed slightly better for most adverse events, a major success was achieved for pump thrombosis, which occurred in 1.4% versus 13.9% of patients. [31]. In addition, gastrointestinal bleeding is reduced (24.5% vs. 30.9%), which is believed to be related to introducing the speed modulation program, the so-called artificial pulse [24].

The HM3 received the CE mark in 2015, and the latest data from Europe confirm a survival rate of 54% after five years. The development of LVAD over the last decades resolved in state-of-the-art third-generation devices, such as the HM3, which play

an essential role in today's treatment of advanced heart failures. Due to their good performance, they are not only considered as a bridge to transplant solutions but also as a promising destination therapy [36]. The following investigations are carried out with the HM3, which is currently the most commonly clinically used device.

1.2 Introduction of the investigated LVAD - Heart-Mate III

As aforementioned, the HM3 is a continuous flow pump with full magnetic levitation and electromagnetic drive. The design of the levitation and drive system is illustrated in Figure 1.3. While the radial position of the impeller is actively controlled, the permanent magnet's attraction of the impeller avoids axial translation or tilting [18]. The fluid is drawn in through the cannula, pumped through the blade channel into the volute, and exits the pump via the outlet. While this flow is considered the primary flow, a secondary flow develops as the fluid moves through the top and bottom gaps, which are shown in Figure 1.2. This secondary flow is driven by the pressure difference developed through the pump and is crucial for the washout of these gaps. The washout is necessary because a long residence time of the blood in the area induced by high shear increases hemolysis, as reported in Section 1.4. Further, Taylor vortices develop due to the relative rotation of the two concentric cylinders, namely the outer housing and the top shroud. To achieve better antithrombogenicity, the surfaces in the volute and cannula are coated with titanium microspheres via sintering [22]. On the rough surface, a higher adhesion of blood platelets is achieved [27], forming a liner, which may lead to fewer thromboembolic events [56].

The impeller consists of four blades and has an inner diameter of 6.7 mm and an outer diameter of 18.7 mm. The blade channel is 3.6 mm in height. The top gap has a radial height of 0.5 mm and an upper height of 1 mm. The bottom gap height is 1.75 mm.

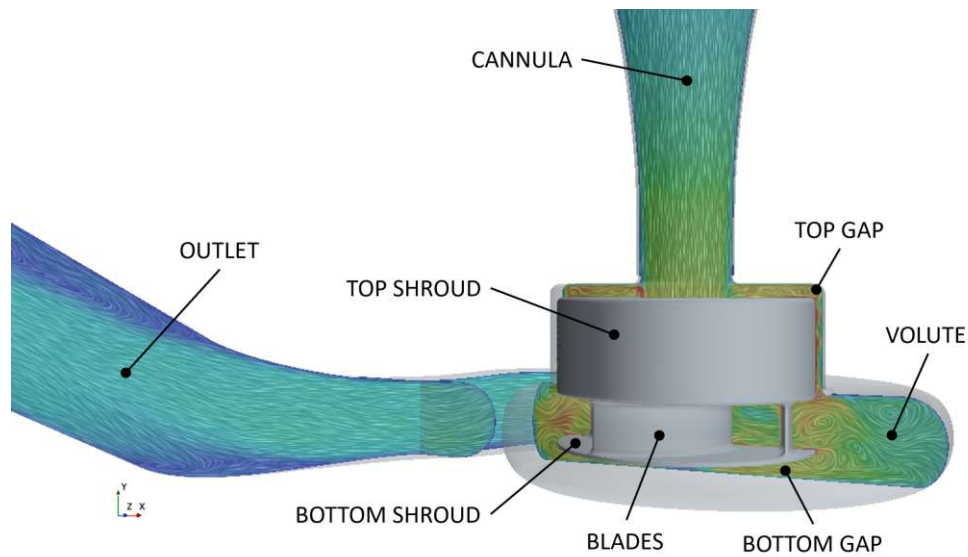


Figure 1.2: Fluid continuum of the HM3, outlining the secondary flow through the top and bottom gap.

1.3 Hemodynamics

Hemodynamics comprises blood flows and pressures in the cardiovascular system, starting with the pulsatile pressure generated by the heart to the forces acting in the blood, e.g. viscous and internal forces, as well as on the elastic vessel walls [43]. As this research focuses on the interaction of the pump with the directly connected cardiac system, two parts of the cardiac system are of specific interest: the left ventricle and the aorta. Figure 1.3 shows the HM3 in tandem with the native heart. The inlet cannula of the pump is situated at the apex of the left ventricle, while the outlet graft is connected to the aorta.

To understand the flow conditions at the pump's in- and outlet, i.e., in the left ventricle and the aorta, the cardiac cycle is considered, particularly the filling and ejection of the ventricle. This mechanism can be divided into the following four phases, see Figure 1.4 [38]:

- Isovolumic contraction: As the contraction begins, the pressure in the ventricle rises above the pressure in the atrium, causing the mitral valve to close. At this point, all valves are closed, and the systole begins. The isovolumic contraction ends with the opening of the aortic valve.

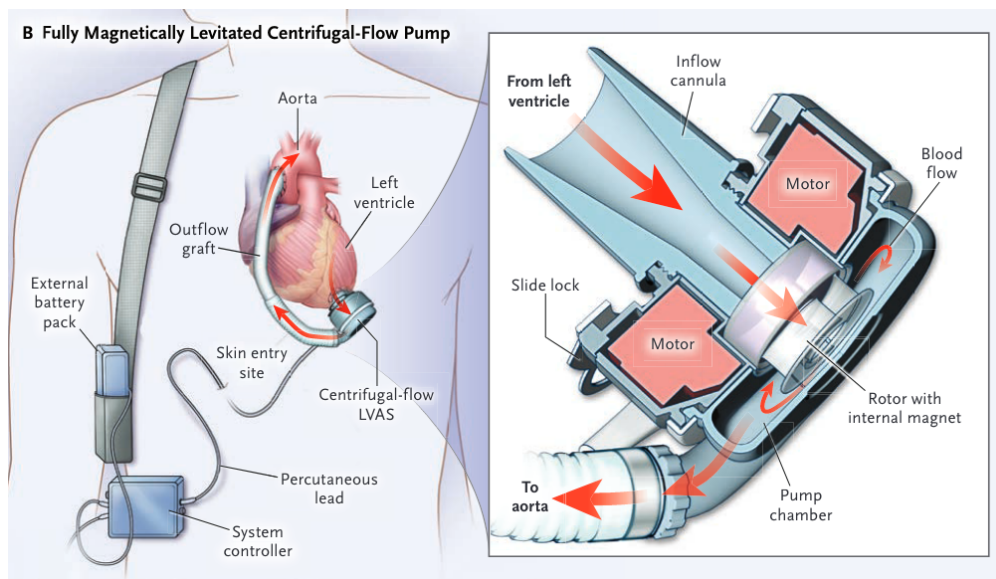


Figure 1.3: Diagram of fully magnetically levitated centrifugal pump. Figure taken from Mehra et al. [30]

- Rapid ventricular ejection: When the pressure in the ventricle exceeds the pressure in the arteries, the aortic valve opens, and approximately 60% of the blood gets ejected.
- Isovolumic relaxation: The mitral and aortic valves are closed. Due to the relaxation, the pressure in the ventricle decreases, which causes the pressure gradient between the blood vessel and the ventricle to rise.
- Ventricular filling: With the mitral valve opening due to the high-pressure gradient, the expanding ventricle gets filled with blood. The relaxation and filling phase is called diastole.

This physiologic mechanism defines the pressure boundary conditions for the pump. The resulting flow rate is determined by the speed setting of the rotating pump impeller, which can be individually adjusted to the patient's support requirements. Using the static characteristic curves of a pump, defined by the head pressure versus flow diagram (HQ diagram) as shown in Figure 1.5, the resulting flow rate can be read for each speed setting.

The characteristic curves are different for each pump, and their shape is important for hemodynamics. A rather flat curve is more pressure-sensitive, resulting in a wide range of flow rates for the pulsatile head pressure given by the ventricular

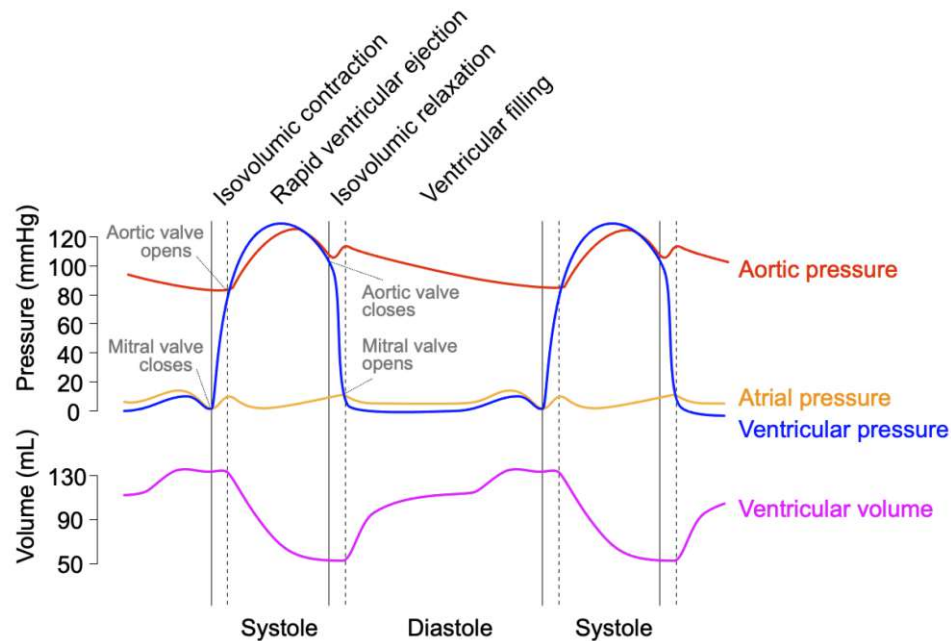


Figure 1.4: Wiggers diagram illustrating the volume and pressures of the blood vessels during the four phases of the cardiac cycle. Figure by Simon Klocker, which is the revised work from Wikimedia Commons.

pressures via a cardiac cycle. This higher pulsatility in flow is often related to higher aortic pressure changes, often regarded as a therapeutic advantage [34]. Furthermore, a steep characteristic curve in low-flow regions is critical, as pressure peaks occur, which can lead to suction of the ventricular wall into the pump's inlet [34]. While it was long believed that axial pumps have steeper characteristic curves than centrifugal pumps, Boes et al. have shown that this is not generally the case [3].

1.3.1 Static characteristics

With the principle of turbomachinery and considerations of hydraulic losses, a universal model for rotodynamic blood pumps can be formulated [3]. The ideal head pressure for a rotodynamic pump with incompressible fluid is given by the EULER's equation

$$H_{EUL} = u_2(u_2 + c_{m2} \cot(\beta_2)) \quad (1.1)$$

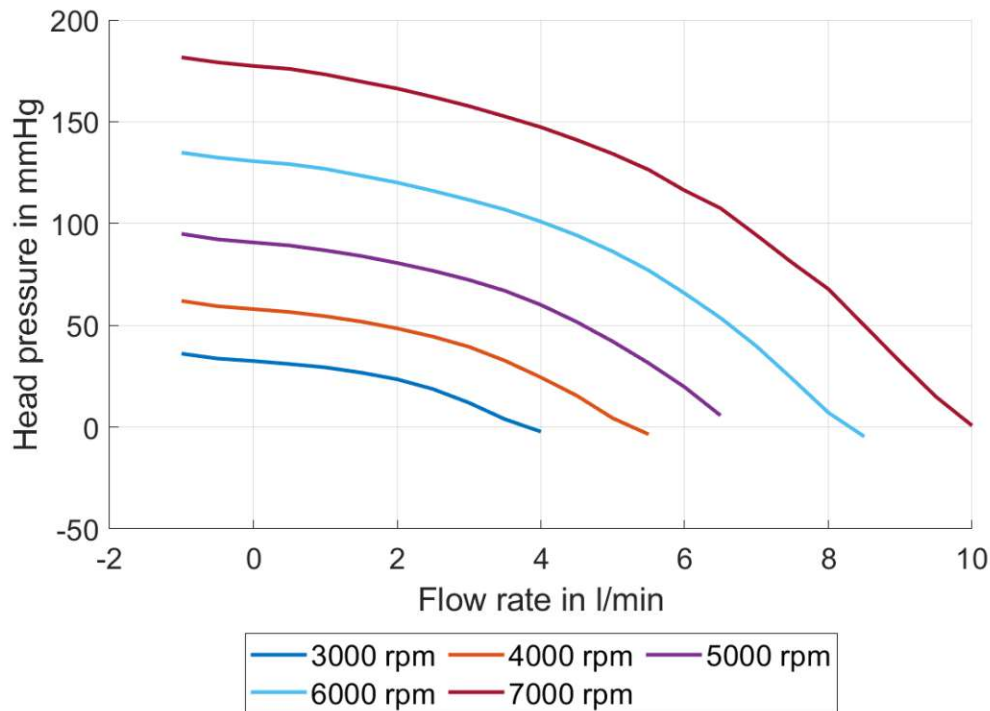


Figure 1.5: Static characteristics (HQ diagram) of the HM3 for various speed settings.

with the circumferential discharge velocity u_2 , the meridional discharge velocity c_{m2} (referring to the component of the absolute velocity normal to the peripheral velocity) and the discharge angle β_2 [48]. To formulate the hydraulic model, equation [1.1] is transformed by combining the variables that are independent of the flow rate and velocity [3]

$$H_{EUL} = K_1 n^2 + K_2 n Q . \quad (1.2)$$

The friction, diffusion, and incidence losses are considered to achieve a more realistic model. The friction losses, in general, can be described as

$$H_{fri} = f \frac{L}{4m} \frac{u^2}{2g} , \quad (1.3)$$

where f is the friction factor, L the characteristic length, m the hydraulic radius, and u the velocity. Complex geometries, such as pumps, require a subdivision into sections, for which equation [1.3] is applicable. In addition, the selection of friction parameters is a challenge in itself. Therefore, it is suitable to summarise all the

friction losses for each section in one term described by the factor $K_{3,fri}$

$$H_{fri} = K_{3,fri}^* \frac{v_1^2}{2g} = K_{3,fri} Q^2 . \quad (1.4)$$

Analogous, the diffusion losses behave in the same way and can be combined into one equation

$$H_{fri} = (K_{3,fri} + K_{3,diff}) Q^2 = K_3 Q^2 \quad (1.5)$$

with the constant K_3 for a given pump [48].

Besides the friction and diffusion losses, incidence losses exist. Due to off-design incidence angles, sudden expansion or diffusion can occur after separation at the blade channel inlet, which causes hydraulic losses. These types of losses are also referred to as eddy and separation losses. Consequently, there is a flow rate Q_{des} at which the flow direction agrees with the entrance and exit blade angle. A deviation from this flow rate Q_{des} in any direction will lead to an additional diffusion loss and can be expressed as

$$H_{inc,1} = K_{4,1} \frac{\Delta c_{u1}^2}{2g} \quad (1.6)$$

for the entrance and as

$$H_{inc,2} = K_{4,2} \frac{\Delta c_{u2}^2}{2g} \quad (1.7)$$

for the discharge. Finally, they can be combined with the constant K_4 as [48]

$$H_{inc} = K_4 (Q - Q_{des})^2 . \quad (1.8)$$

Since the designed flow rate Q_{des} depends linearly on the speed of the impeller, the equation [1.8] can be rewritten as

$$H_{inc} = K_4 (Q - K_7 n)^2 = K_5 Q^2 - K_6 n Q + K_7 n^2 . \quad (1.9)$$

A frequently disregarded effect is the part load circulation at the impeller inlet. This effect occurs at low flow and intensifies towards zero flow. Due to recirculation, the outer part of the inlet cross section gets blocked, which is the effective diameter of the inlet. The head pressure increases by the amount [16]

$$H_{rec} = \frac{u_2^2}{2g} \left(\frac{d_1^2}{d_2^2} - \frac{d_{1,eff}^2}{d_2^2} \right) . \quad (1.10)$$

Assuming firstly that the diameter changes linearly with the flow rate and secondly that the effective diameter can be approximated by a linear function of the velocity, the equation [1.10](#) becomes

$$H_{rec} = K_8(Q^2 - q_{inf}^2) = K_8(Q^2 - K_9n^2) . \quad (1.11)$$

Finally subtracting [1.4](#)[1.9](#) and adding [1.11](#) from [1.2](#) the head pressure can be modelled as

$$H = H_{EUL} - H_{fri} - H_{inc} + H_{rec} , \quad (1.12)$$

respectively

$$H = an^2 - R_1nQ - R_2Q^2 + \begin{cases} 0 & Q > q_{inf} \\ R_{rec}(Q^2 - q_{inf}^2) & Q < q_{inf} \end{cases} , \quad (1.13)$$

where a, R_1, R_2, R_{rec} result from combining the constant $K_1 - K_9$ [3](#).

These constants can be determined for a given pump using experimental data. This has been done for the HM3; the result is shown in Figure [1.6](#).

1.3.2 Dynamic characteristics

So far, only static characteristic curves have been discussed in prior sections. A certain head pressure results in a flow rate at a certain impeller speed. However, during a cardiac cycle, the head pressure changes. Furthermore, due to the inertia of the fluid, the change in head pressure is not immediately reflected in the flow rate. A certain amount of time is required to accelerate or decelerate the fluid. Therefore, the change is not moving on the static characteristic curve but on a loop counterclockwise around this curve, as shown in the measured data in Figure [1.7](#). During systole, the fluid is accelerated and lags behind the static curve. In contrast, the fluid slows down during diastole, and while at the beginning, the deceleration matches the static characteristics, the dynamic curve divides with the flattening of the static characteristics.

This time dependency can be included in the hydraulic model [1.13](#) by adding

$$H_{dyn} = \rho \frac{L_{eq}}{A_{eq}} \frac{dQ}{dt} , \quad (1.14)$$

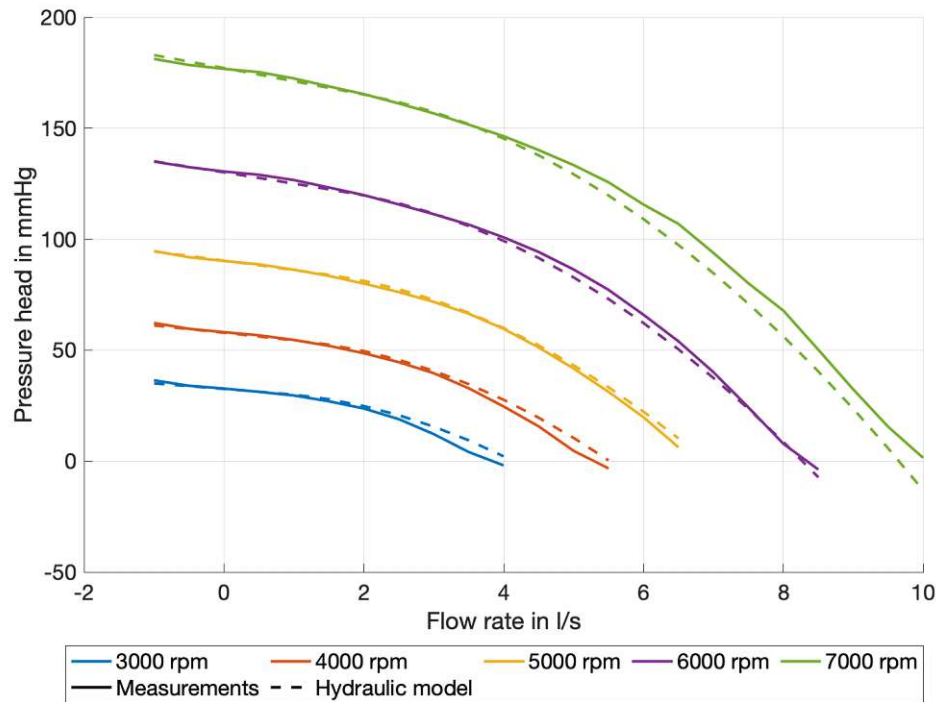


Figure 1.6: Measured static characteristics versus fitted hydraulic model of the HM3 for various speed settings show good agreement.

where L_{eq} and A_{eq} represent the dimensions of an equivalent pipe [52], and with combined constants as

$$H_{dyn} = L_{in} \frac{dQ}{dt} . \quad (1.15)$$

The final dynamic hydraulic model reads [3]

$$H = an^2 - R_1nQ - R_2Q^2 + L_{in} \frac{dQ}{dt} + \begin{cases} 0 & Q > q_{inf} \\ R_{rec}(Q^2 - q_{inf}^2) & Q < q_{inf} \end{cases} . \quad (1.16)$$

Figure 1.8 compares the fitted hydraulic model with measured data for the HM3.

1.4 Hemocompatibility

As mentioned previously, adverse events such as bleeding, strokes and pump thrombosis continue to pose a clinical challenge, and pump-specific flow phenomena are associated with such adverse events. Not only the damage of blood components

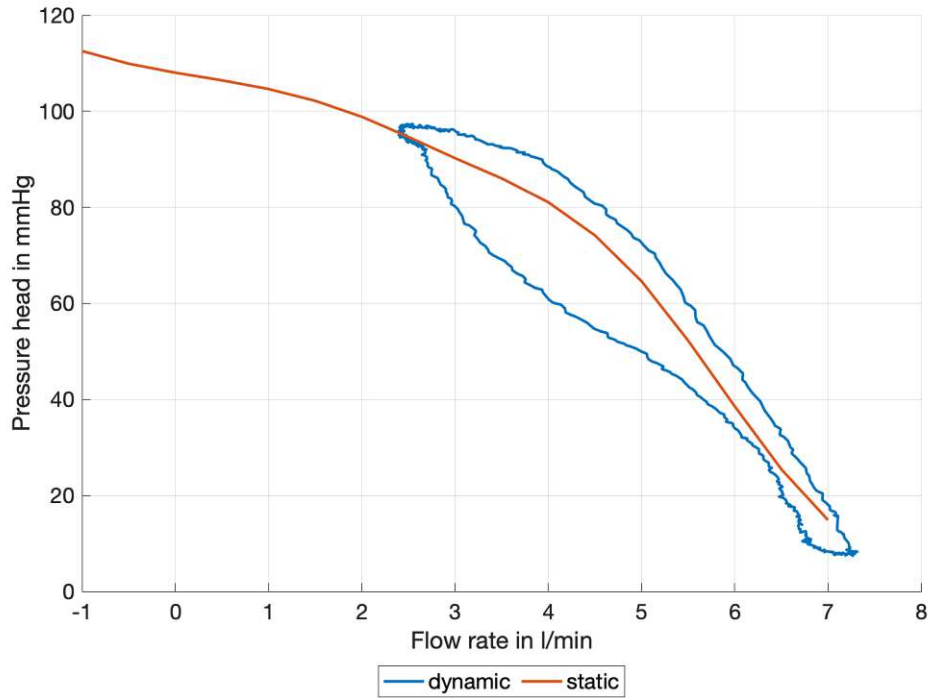


Figure 1.7: Measured dynamic characteristics of HM3, performing a clockwise loop around the static characteristic at 5400 *rpm* due to inertia effects.

themselves but also the activation of platelets and the aggregation of blood particles are results of shear acting on the components. Moreover, not just the shear stress magnitude alone has to be considered, but also the exposure duration. These considerations can be formulated for the case of red blood cell damage, which is called hemolysis, in the power law introduced by Giersiepen et al. [14]

$$HI[\%] = \frac{fHb}{Hb} \cdot 100 = C\tau^{\alpha}t_{exp}^{\beta} \quad (1.17)$$

with the free hemoglobin fHb , that is released by damaged red blood cells, the total hemoglobin Hb of the blood, the shear stress τ , the exposure time t_{exp} and the empirical regression coefficients C , α and β .

Consequently, knowledge about shear rates and residence times is crucial for predicting hemolysis. While these parameters can only be measured globally without knowledge of local effects, CFD offers an elegant approach for local investigations.

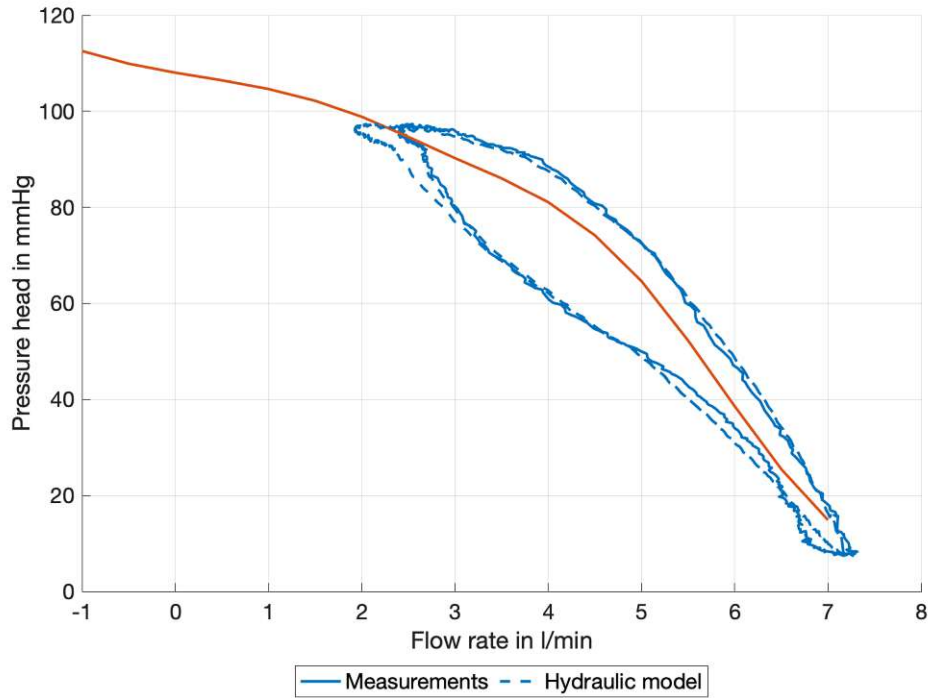


Figure 1.8: Measured dynamic characteristics versus modeled characteristics of the HM3 at 5400 *rpm* show overall good agreement.

1.5 Principles of computational fluid dynamics

The basic laws of fluid dynamics are conservation of mass [1.18](#), momentum [1.19](#) and energy [1.20](#)

$$\frac{\delta \rho}{\delta t} + \nabla \cdot \rho \mathbf{u} = 0, \quad (1.18)$$

$$\frac{\delta \rho \mathbf{u}}{\delta t} + \nabla \cdot (\rho \mathbf{u} \otimes \mathbf{u}) = \rho \mathbf{f}_e + \nabla \cdot (-p \bar{\bar{I}} + \bar{\bar{\tau}}), \quad (1.19)$$

$$\frac{\delta \rho E}{\delta t} + \nabla \cdot (\rho H_{tot} \mathbf{u} - k \nabla T - \bar{\bar{\tau}} \cdot \mathbf{u}) = W_f + q_H, \quad (1.20)$$

where

- ρ is the density,
- ∇ is the divergence operator,
- \mathbf{u} is the velocity vector,
- \mathbf{f}_e is the vector of external forces,

- $\bar{\bar{I}}$ is the identity matrix,
- $\bar{\bar{\tau}}$ is the stress tensor,
- E is the total energy,
- H_{tot} is the total enthalpy,
- T is the temperature,
- W_f is the work of external forces and
- q_H is the external heat,

giving a set of five coupled equations. Additional equations obtained from the investigated fluid are necessary to close this system of equations. In our case, the fluid is blood or a blood analogue. While blood is a non-Newtonian fluid (see Figure 1.9), the analogue blood behaves like a Newtonian fluid. As blood analogue

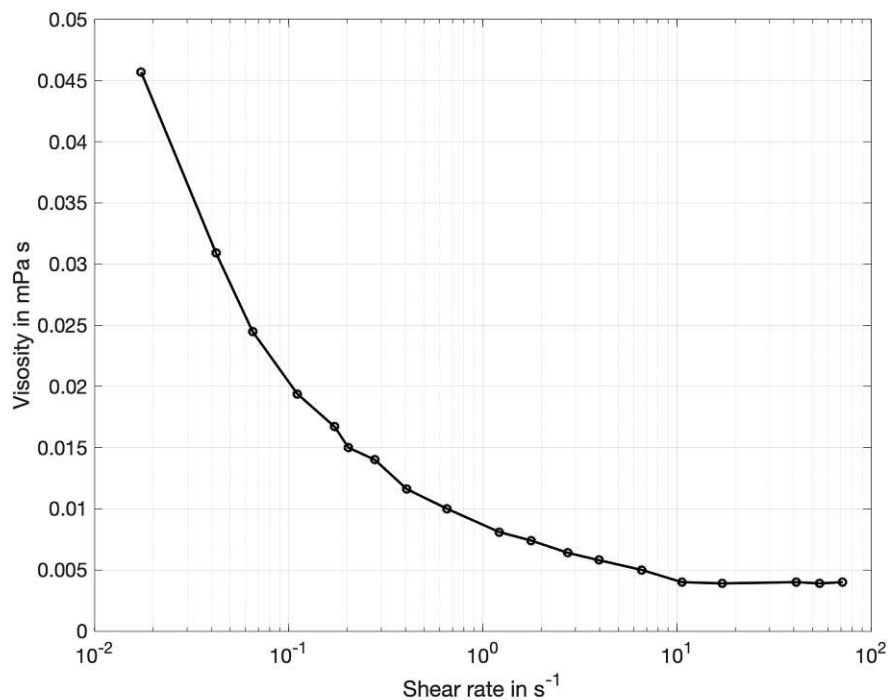


Figure 1.9: Non-Newtonian behaviour of blood [5].

is incompressible,

$$\frac{\delta \rho}{\delta t} + \mathbf{u} \cdot \nabla \rho = 0, \quad (1.21)$$

the set of equations (1.18-1.20) simplify to (1.21)

$$\nabla \cdot \mathbf{u} = 0 , \quad (1.22)$$

$$\frac{\delta \mathbf{u}}{\delta t} + \mathbf{u} \cdot \nabla \mathbf{u} = -\frac{\nabla p}{\rho} + \nu \nabla^2 \mathbf{u} + \mathbf{f}_e \quad (1.23)$$

and decouple from the conservation of energy. Equation (1.23) contains a system of equations known as the incompressible Navier-Stokes equations. Note that the equation system has four unknowns and is still coupled.

Since we want to numerically solve this system of equations, space and time must be discretised. This is done by dividing the space continuum into small domains, creating a mesh, and defining a time step. Structured and unstructured meshes can be used for spatial discretisation. While a uniform, structured mesh aligned with the main flow features provides the best accuracy, creating structured meshes for complex geometries can be difficult and time-consuming. Therefore, using an unstructured mesh and proof sufficiently fine resolution can be more suitable. To ensure that the discretisation does not falsify the solution, mesh independence and time independence must be verified.

Several methods exist for solving the system (1.22-1.23). On the one hand, the system can remain coupled, which can be beneficial for compressible flow, or the equations can be solved sequentially (segregated flow) to reduce the memory requirement, as done in this thesis. The transient solvers in Simcenter STAR CCM+ (Siemens Digital Industries Software, USA) provided for segregated flow are *PISO unsteady*, *Implicit unsteady*, and *Explicit unsteady*. Implicit solvers are generally used for stability and robustness reasons with larger time steps. The *PISO unsteady* algorithm is explained here as an example (20).

First, PISO stands for "Pressure Implicit with Splitting Operator" and consists of a predictor step followed by two corrections steps. The discretised momentum equation can be written as

$$\frac{\rho}{\delta t} (u_i^{n+1} - u_i^n) = H(u_i^{n+1}) - \Delta_i p^{n+1} + S_i , \quad (1.24)$$

where δt is the discretised time step, the operator H represents the spatial finite-difference of the flux, Δ_i the finite-difference equivalent of the gradient and S_i the external source of momentum. The superscript represents the iteration, while *, **, *** in the following indicate intermediate values during the splitting algorithm.

1. Predictor step: the prevailing pressure and velocity field is used to calculate u_i^* implicitly

$$\frac{\rho}{\delta t}(u_i^* - u_i^n) = H(u_i^*) - \Delta_i p^n + S_i . \quad (1.25)$$

2. First corrector step: Since u_i^* will not satisfy the zero-divergence [1.22](#), the velocity field must be corrected. Applying the zero-divergence criterion of a newly defined velocity field u^{**}

$$\Delta_i u^{**} = 0 \quad (1.26)$$

for the now explicit momentum equation

$$\frac{\rho}{\delta t}(u_i^{**} - u_i^n) = H(u_i^*) - \Delta_i p^* + S_i \quad (1.27)$$

leads to

$$\Delta_i^2 p^* = \Delta_i u_i^* + \Delta_i S_i + \frac{\rho}{\delta t} \Delta_i u_i^n . \quad (1.28)$$

The pressure field p^* obtained by solving [1.28](#) can be reinserted in [1.27](#) to calculate the divergence free velocity field u^{**} .

3. Second corrector step: the corrector step can be repeated with the new divergence-free velocity field u^{***} to yield the pressure field p^{**}

$$\Delta_i u^{***} = 0 \quad (1.29)$$

$$\frac{\rho}{\delta t}(u_i^{***} - u_i^n) = H(u_i^{**}) - \Delta_i p^{**} + S_i , \quad (1.30)$$

respectively

$$\Delta_i^2 p^{**} = \Delta_i u_i^{**} + \Delta_i S_i + \frac{\rho}{\delta t} \Delta_i u_i^n . \quad (1.31)$$

Although additional corrector steps are possible, Issa showed that two corrector steps are mostly sufficient to approximate the exact solution for u_i^{n+1} and p^{n+1} [20](#). Subsequently, the time step can be updated, and the PISO algorithm can be repeated.

Turbulence is often assumed to occur in rotodynamic blood pumps [11](#), [25](#), [50](#), [51](#), [54](#). The modelling approach used in this thesis is the **R**eynolds **A**veraged **N**avier **S**tokes equation (RANS). The model is based on the Reynolds decomposition, which divides the velocity into a time-averaged part \bar{u} and an additional fluctuation

u' to account for turbulence [1]

$$u(\mathbf{x}, t) = \bar{u}(\mathbf{x}) + u'(\mathbf{u}, t) . \quad (1.32)$$

While the additional term disappears in the conservation of mass [1.22] due to time averaging

$$\frac{\partial \bar{u}_i}{\partial x_i} = 0 , \quad (1.33)$$

the additional term $\frac{\partial \overline{u'_i u'_j}}{\partial x_j}$ remains in the momentum equation [1.23]

$$\frac{\partial \bar{u}_i}{\partial t} + \bar{u}_j \frac{\partial \bar{u}_i}{\partial x_j} = -\frac{1}{\rho} \frac{\partial p}{\partial x_j} + \nu \frac{\partial^2 \bar{u}_i}{\partial x_i \partial x_j} - \frac{\partial \overline{u'_i u'_j}}{\partial x_j} . \quad (1.34)$$

This term is also called *Reynolds stress*, and consequently, the *Reynolds stress tensor* is formed

$$\tau_{turb} = \begin{bmatrix} \overline{u'u'} & \overline{u'v'} & \overline{u'w'} \\ \overline{v'u'} & \overline{v'v'} & \overline{v'w'} \\ \overline{w'u'} & \overline{w'v'} & \overline{w'w'} \end{bmatrix} . \quad (1.35)$$

Considering the symmetry ($\overline{u'_i u'_j} = \overline{u'_j u'_i}$) the system gets 6 new unknowns. With \bar{u}_i and p , the number of unknowns adds up to a total of 10, while the system consists of 4 equations, which results in a closure problem.

To deal with it, the most common approach is the *Boussinesq hypothesis*, which reads for incompressible flow

$$-\overline{u'_i u'_j} = \nu_t \left(\frac{\partial \bar{u}_i}{\partial x_j} - \frac{\partial \bar{u}_j}{\partial x_i} \right) - \frac{2}{3} k \delta_{ij} , \quad (1.36)$$

where ν_t is the turbulent eddy viscosity, $k = \frac{1}{2} \overline{u'_i u'_i}$ the turbulent kinetic energy and δ_{ij} the *Kronecker delta*. The system can be solved by introducing new transport equations for the turbulent eddy viscosity and the turbulent kinetic energy, although the solution represents an approximation. Since the turbulent eddy viscosity is an empirical quantity, it must be converted to transfer it into a transport equation. This is done by introducing the dissipation rate

$$\epsilon = C_\mu \frac{\rho k^2}{\mu_t} = C_\mu \frac{k^2}{\nu_t} , \quad (1.37)$$

where $C_\mu = 0.09$ is an empirically fitted constant. Different turbulence models use different transport equations. The best known are *Spalart-Allmaras* [47] as a representative for one equation models and $k - \epsilon$ [8] and $k - \omega$ [55] or $k - \omega SST$ [32] as representatives for two equation models. The following explains the basic idea of the $k - \epsilon$ model.

The transport equation for the turbulent kinetic energy is

$$\rho \frac{\partial k}{\partial t} + \rho \bar{u}_j \frac{\partial k}{\partial x_j} = \frac{\partial}{\partial x_j} \left[\mu + \frac{\mu_t}{\sigma_k} \frac{\partial k}{\partial x_j} \right] + P_k - \rho \epsilon + P_b + S_k, \quad (1.38)$$

where P_k is the production due to mean velocity shear, P_b is the production due to buoyancy and S_k is a user-defined source. For the dissipation rate, the transport equation reads

$$\begin{aligned} \rho \frac{\partial \epsilon}{\partial t} + \rho \bar{u}_j \frac{\partial \epsilon}{\partial x_j} &= \frac{\partial}{\partial x_j} \left[\mu + \frac{\mu_t}{\sigma} \frac{\partial \epsilon}{\partial x_j} \right] + \dots \\ C_1 \frac{\epsilon}{k} \left(\tau_{ij} \frac{\partial \bar{u}_i}{\partial x_j} + C_3 P_b \right) &- C_2 \frac{\epsilon^2}{k} C_\mu \rho \mu_t \left(\frac{\partial \bar{u}_i}{\partial x_j} + \frac{\partial \bar{u}_j}{\partial x_i} \right) \frac{\partial \bar{u}_i}{\partial x_j} - C_2 \rho \frac{\epsilon^2}{k} + S_\epsilon, \end{aligned} \quad (1.39)$$

where $\sigma_k, \sigma, C_1, C_2$ and C_3 are additional empirical model coefficients. After solving the transport equations [1.38] and [1.39], the turbulent eddy viscosity ν_t , or μ_t can be calculated using equation [1.37]. The $k - \epsilon$ model only works in regions with high Reynolds numbers (see section [2.1.6]), and therefore not in near-wall regions. To compensate for that, empirical wall functions can be used [29]. Since these empirical functions are not accurate in the presence of adverse pressure gradients, an alternative is to use a so-called $k - \omega$ model, which does not require additional empirical wall functions, where the specific eddy viscosity ω is

$$\omega = \frac{\epsilon}{C_\mu k}. \quad (1.40)$$

Both, ϵ and ω , represent the rate at which kinetic energy is converted into thermal energy and can therefore be converted at any time. While the transport equation for the turbulent kinetic energy k stays unchanged, the transport equation for ω reads

$$\rho \frac{\partial \omega}{\partial t} + \rho \bar{u}_j \frac{\partial \omega}{\partial x_j} = \frac{\partial}{\partial x_j} \left[\mu + \sigma \mu_t \frac{\partial \omega}{\partial x_j} \right] + \alpha \frac{\omega}{k} C_\mu \rho \mu_t \left(\frac{\partial \bar{u}_i}{\partial x_j} + \frac{\partial \bar{u}_j}{\partial x_i} \right) \frac{\partial \bar{u}_i}{\partial x_j} - \beta_\omega \rho \omega^2 + S_\omega, \quad (1.41)$$

where σ , α and β are empirical model coefficients. Although the $k - \omega$ model is more accurate and robust in near-wall regions, especially in the presence of adverse pressure gradients, it is highly dependent on the free stream turbulent condition due to numerical reasons [21]. By blending the $k - \epsilon$ model, which is superior in the free stream, with the $k - \omega$ model, a more universal model can be formulated. This was done by Menter, who introduced the well-known *Menter's $k - \omega$ SST model* in 1994 [32], which is also the model used in this thesis and in most literature investigating rotodynamic blood pumps [11, 25, 50, 51, 54].

1.6 State-of-the-art

1.6.1 Static characterisation of rotodynamic blood pumps

Currently, numerical investigations using CFD are well established in rotodynamic blood pump design, first and foremost to guarantee the hydraulic performance but also to investigate blood trauma. In previous literature, computational fluid dynamics has often been used for flow investigations, especially to predict hemolysis. Not only have experimental validations been performed using different fluid properties, but a variety of simulation setups (e.g. interface, turbulence, motion modelling) have been used. Figure 1.10 compares published static hydraulic characteristics of the HM3 gained from experimental data by measuring the flow rate and the head pressure across the pump. While Boes et al. [3], Escher et al. [11] and Wiegmann et al. [54] use a water-glycerol mixture (47 mass-% glycerol, at 37°C , 3 mPa , 1110 kg/m^3) to match the dynamic viscosity of blood, Thoratec does not mention the working fluid [18]. Table 1.1 lists the used densities and dynamic viscosities. All published characteristics, except Escher et al., agree very well, although different test benches were used. Escher et al. substantially modified the pump to implement a torque measurement, which could explain the deviation [11].

As observable in Figure 1.11, the numerical predictions agree well with the experimental data. The characteristics equation 1.16 is independent of the density. However, since all publications use the head pressure, which is

$$H_{pres} = H_{length} \rho g \quad (1.42)$$

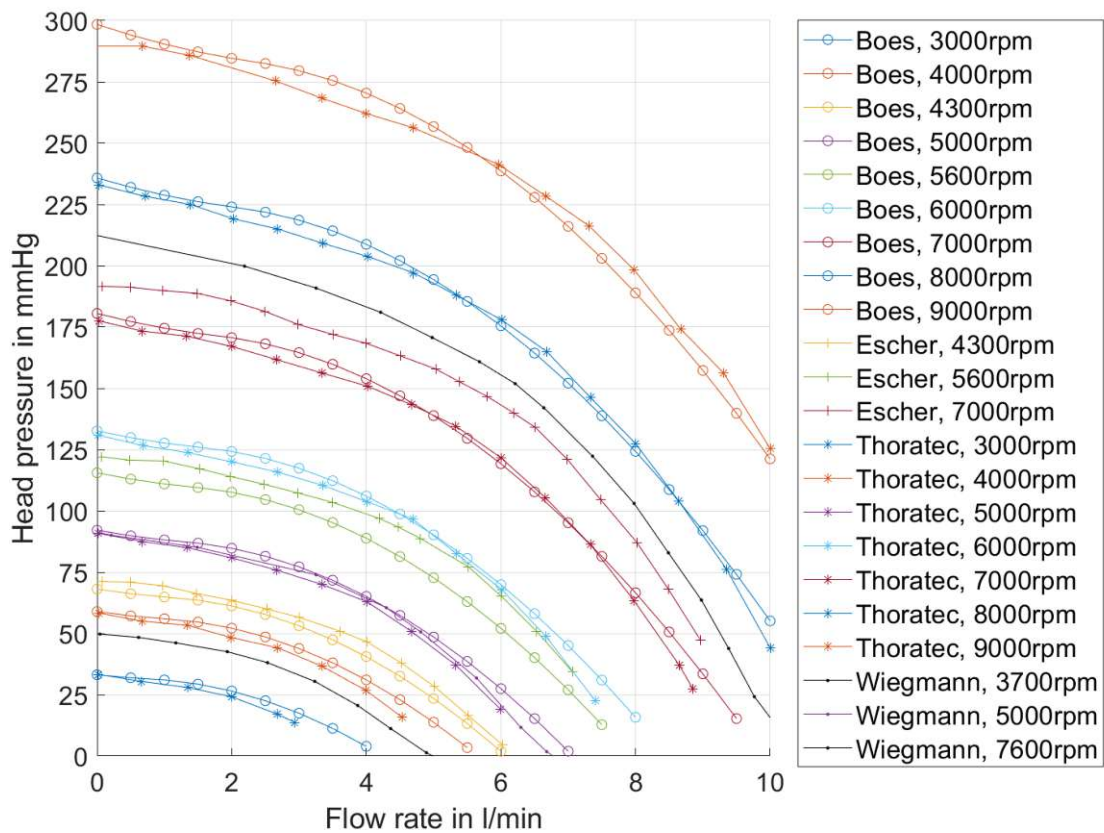


Figure 1.10: Published static characteristics obtained from experimental data at various speed settings with overall good agreement except Escher et al.

using the fluid density ρ , it becomes obvious that it scales the head pressure linearly. As most publications used a water-glycerol mixture as a blood analogous in experiments, the resulting density of the working fluid differs from the density of blood that is used in CFD, see [1.1](#).

Only Escher et al., 2023 [\[11\]](#) used the same fluid properties for experimental and numerical investigations. Their numerical predictions overestimate the experimental data slightly. In [Figure 1.12](#), the published numerical results were linearly corrected according to equation [1.42](#). Note that the linear correction is a rough assumption as additional effects (friction, turbulence, etc.) are added. Nevertheless, a clear overestimation is visible.

The actual influence of density is shown in [Figure 1.13](#) using two comparable numerical setups with different fluid properties [\[10\]](#), [\[11\]](#). This leads to the first

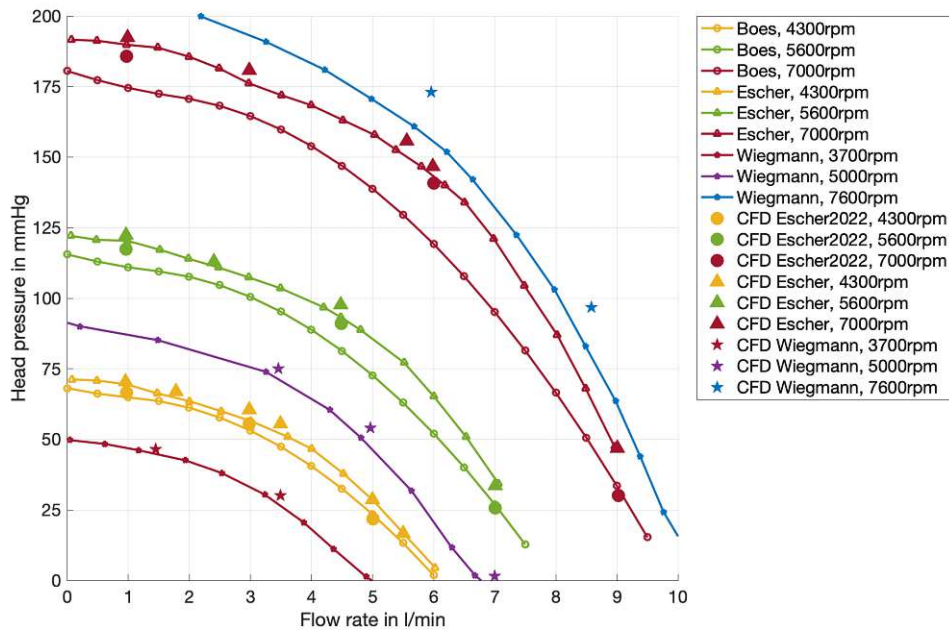


Figure 1.11: Published static characteristics obtained from experiments, along with numeric results. Escher et al. (2022) compare the numeric results with the experimental data from Boes et al.

objective of this thesis:

Establishing a numerical flow simulation methodology and benchmark solutions for the HM3 rotodynamic blood pump at static operating conditions by validating experiments using the same fluid properties.

1.6.2 Dynamic characterisation of rotodynamic blood pumps

Since the static characteristics do not adequately describe the actual realistic operating state in clinical applications, taking the dynamic behaviour, represented

Table 1.1: Fluid properties used in literature

	EXP		CFD	
	ρ in $\frac{kg}{m^3}$	μ in $mPa s$	ρ in $\frac{kg}{m^3}$	μ in $mPa s$
Escher 2022	1110.0	3.0	1050.0	3.5
Escher 2023	1110.0	3.0	1110.0	3.0
Wiegmann	1110.0	3.0	1050.0	3.5

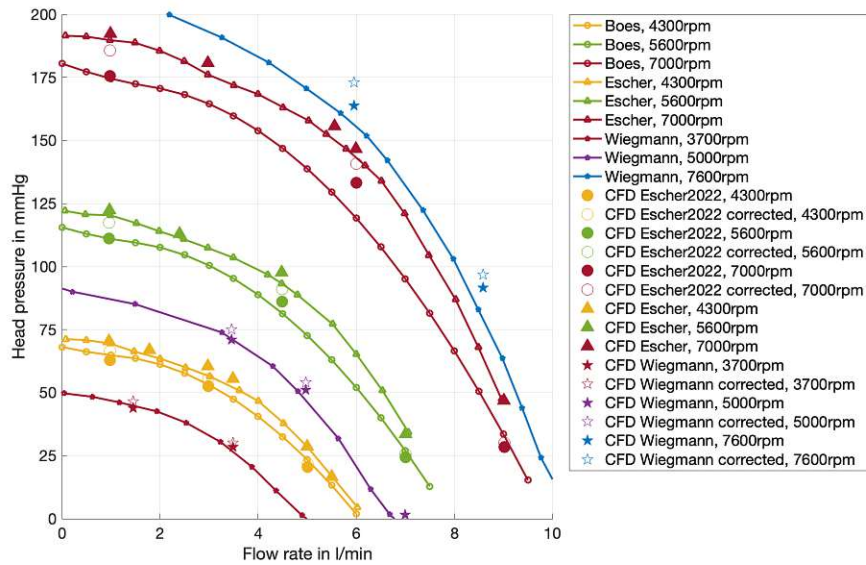


Figure 1.12: Linear correction of published numerical results to compensate for approximated errors due to deviating fluid properties results in a larger deviation between measured and predicted static characteristics.

by the dynamic HQ curve, into account can lead to a better prediction of hemocompatibility. [35]. For this, a validated numerical simulation setup is fundamental. Recent publications have addressed dynamic numerical investigations, but none of them has been validated with in-vitro-generated dynamic HQ curves using the same fluid properties. The different setups are listed in table 1.2. Therefore, the second subsequent objective of this thesis is:

Establishing a numerical flow simulation methodology and benchmark solutions for the HM3 rotodynamic blood pump at dynamic operating conditions by validating experiments using the same fluid properties.

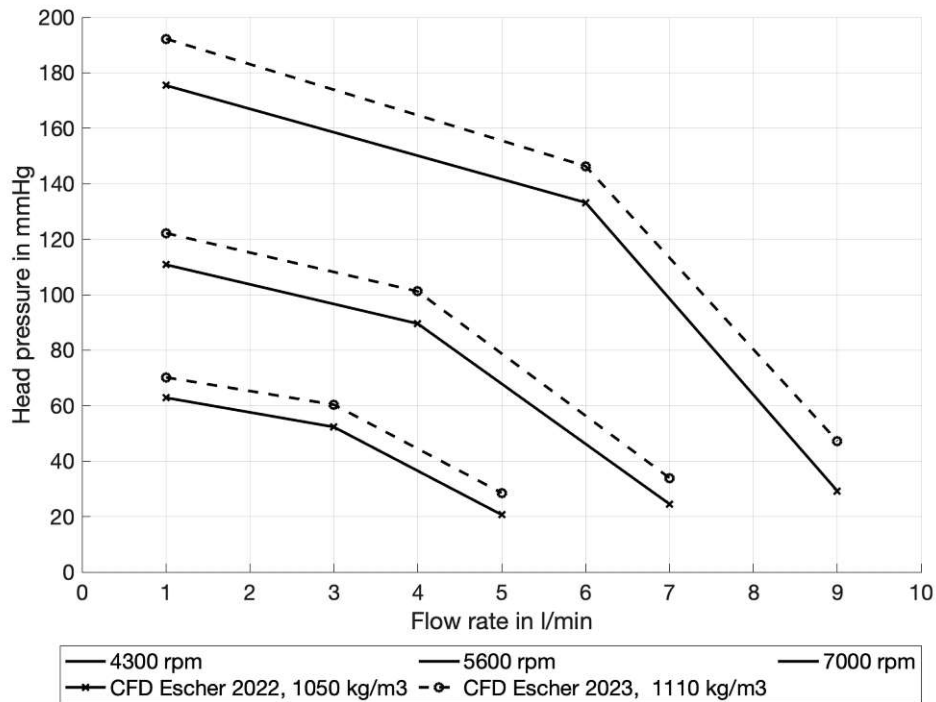


Figure 1.13: Influence of density on numerical results of two comparable published numerical simulation setups with different fluid properties. [10], [11]

Table 1.2: Literature overview of numerical setups investigating dynamic boundary conditions

Author	Fluid	Boundary condition	Time step	Physical time	Motion	Turbulence	Validation
Song et al. [46]	1050 $kg\ m^{-3}$, 3.5 $mPa\ s$	LVQ, AOP	0.005 s	2 CC	sliding mesh	$k - \epsilon$	n.A.
Li et al. [25]	1059 $kg\ m^{-3}$, 3.5 $mPa\ s$	LVQ, AOP	0.002 s	n.A.	sliding mesh	$k - \omega\ SST$	in-vitro with 1100 $kg\ m^{-3}$, 3.5 $mPa\ s$
Chen et al. [7]	1050 $kg\ m^{-3}$, 3.5 $mPa\ s$	LVQ, AOP	n.A.	10 CC	sliding mesh	$k - \omega\ SST$	n.A.
Grinstein et al. [15]	1060 $kg\ m^{-3}$, n.A.	LVQ, AOP	n.A.	n.A.	n.A.	n.A.	n.A.
Huang et al. [19]	1050 $kg\ m^{-3}$, 3.5 $mPa\ s$	LVP, AOP	0.001 s	6 CC	frozen rotor	$k - \omega\ SST$	static condition in-vitro
Li et al. [26]	1055 $kg\ m^{-3}$, 3.5 $mPa\ s$	LVP, AOP	0.002 s	2 CC	n.A.	$k - \epsilon$	static condition in-vitro
Hahne et al. [17]	1055 $kg\ m^{-3}$, 3.5 $mPa\ s$	LVP, AOP	0.0005 s	3 CC	sliding mesh	$k - \omega\ SST$	hydraulic model [3]
Wiegmann et al. [54]	1050 $kg\ m^{-3}$, 3.5 $mPa\ s$	LVP, AOP	0.0006 s	2 CC	sliding mesh	$k - \omega\ SST$	hydraulic model [3]

LVQ - Left ventricle flow rate, LVP - Left ventricle pressure, AOP - Aorta pressure, CC - Cardiac Cycle

Chapter 2

Objective 1 - Static Investigation

Establishing a numerical flow simulation methodology and benchmark solutions for the HM3 rotodynamic blood pump at static operating conditions by validating experiments using the same fluid properties.

As aforementioned, the numerical and experimental results published by Escher et al. [11] compare well, see Figure 2.1. However, the considered pump was modified significantly in the following aspects:

- **Inlet cannula:** The cannula and upper housing were manufactured from optical glass to facilitate optical measurements. Furthermore, the inlet cannula was designed as a straight tube instead of a conical shape.
- **Mechanically mounted impeller:** Instead of magnetic levitation, the impeller was held by mechanical bearings and driven by an additional shaft. Thereby, torque measurements were possible. For manufacturing reasons, the bottom shroud had to be thickened to connect the shaft via struts. This not only changed the geometry at the bottom shroud and bottom gap but also fixed the position of the impeller in radial and axial directions and avoided speed fluctuation.
- **Volute:** To fit the abovementioned changes, the housing, including the volute, had to be adapted and newly manufactured. This was done without using the rough sintered coating in the original pump housing.

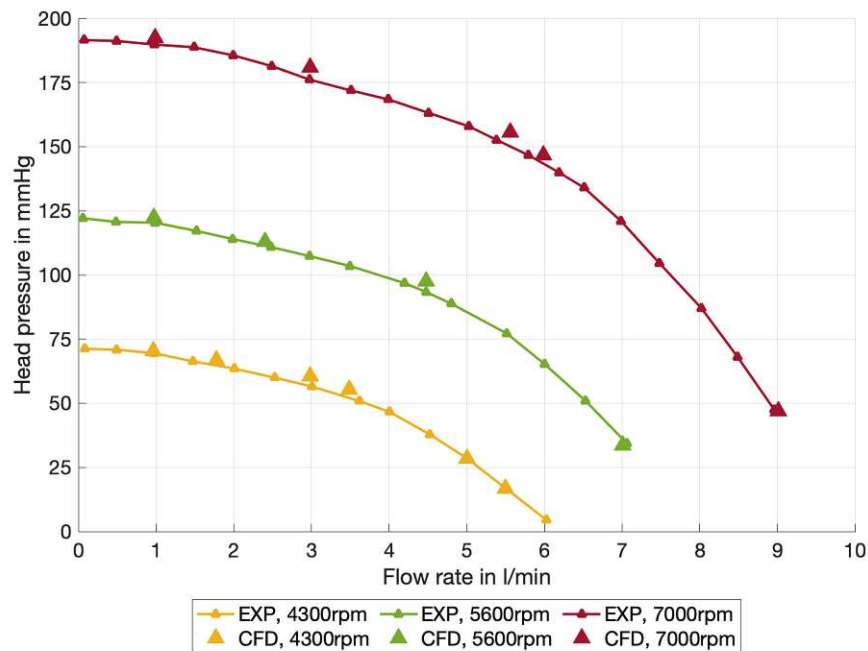


Figure 2.1: Experimental versus numerical results using the same fluid properties published by Escher et al. show good agreement

Escher et al. [11] also compared the modified geometry numerically with the original geometry. Although the flow rate changed in the top and bottom gap, the overall generated head matched ($RMSE = 3.63 \text{ mmHg}$). Consequently, to address the questions where the deviation to the experiments using the original pump stems from, the following investigations can be derived:

- Numerical investigation of the impeller position alongside the influence of different interfaces between the moving and stationary domain
- Numerical investigation of the influence of roughness in the cannula and volute
- Experimental investigation of the influence of the inlet environment, i.e. comparison of mounting the pump directly in the reservoir versus using a straight tube in front of the cannula

In addition, the influence of the numerical implementation of the impeller rotation and turbulence is investigated.

2.1 Methods

2.1.1 Experimental Setup

The experimental mock loop based on Bender et al. [2], shown in [2.2], consists of two pressure-controlled reservoirs representing the left ventricle and the aorta, the LVAD under investigation between them, and a separate gear pump (UP3-R 24V, MARCO s.p.a., Italy) to regulate the mass flow rate. The LVAD is directly mounted in the left ventricle reservoir to mimic physiologic conditions. The outlet graft has a length of approximately 20 cm and enters the aortic reservoir. Upstream of the aortic reservoir, the mass flow rate is measured with a clamp on ultra-sonic flow meter (SONOFLOW® CO.55, SONOTEC GmbH, Germany). Pressure sensors are situated in the reservoirs and 30 mm downstream of the pump outlet to observe the pressure. As the fluid properties depend on the operating temperature, a heat exchanger is placed downstream of the aortic reservoir and the gear pump and set to 37 °C. Furthermore, modifications were made to the pump housing. The lower half of the volute was replaced by acrylic glass to allow optical measurements [50]. Consequently, the lower volute surface is smooth instead of the rough surface of the sintered coating. A hall sensor is employed to get accurate rotational speed measurements in addition to the speed estimation from the HM3 controlling system itself. This setup is referred to as *modVolute*.

The gear pump is controlled for static operation to deliver the desired volume flow while the speed under investigation is selected for the pump. Consequently, the resulting head pressure is measured between the pressure sensors in the left ventricular reservoir and behind the LVAD outlet.

All experiments were done using a water-glycerol mixture (50.7 mass % glycerol) with a dynamic viscosity of 3.5 mPa s and a density of 1120 $\frac{kg}{m^3}$.

2.1.2 Setup with modified Inlet

In another setup, referred to as *modInlet*, an unmodified HM3 was used. A 20 cm long tube was installed between the reservoir and the inlet cannula to investigate the influence of the inlet flow condition. The inlet tube is equipped with additional pressure sensors located 1 cm and 15 cm upstream of the inlet cannula. With the

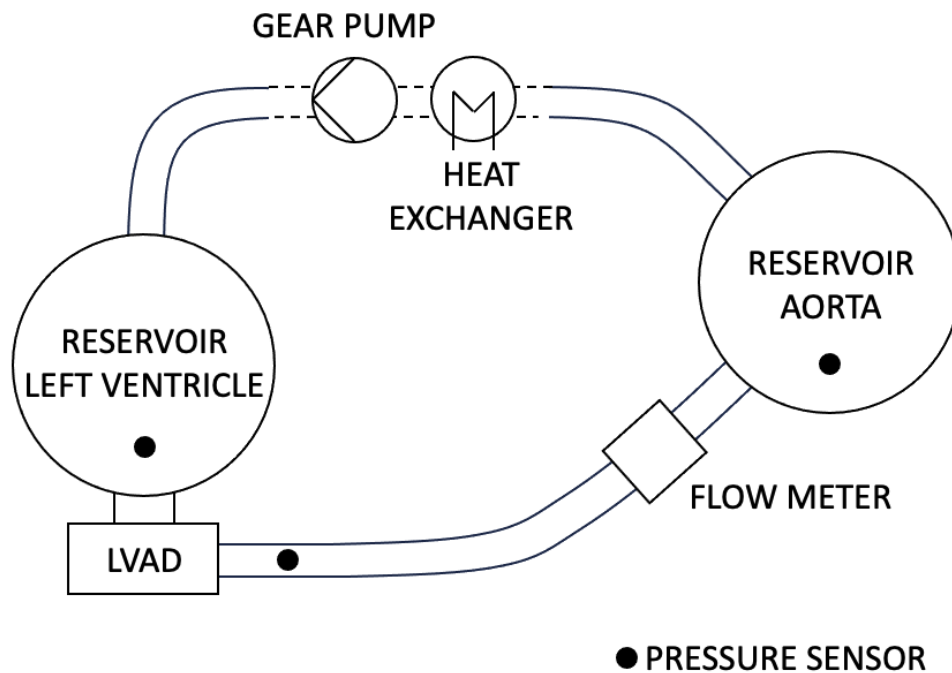


Figure 2.2: The experimental mock loop setup involves directly mounting the LVAD onto the left ventricular reservoir, followed by a 20 cm outlet graft leading into the aortic reservoir. A flow meter is positioned upstream of the aortic reservoir, and pressure sensor locations are indicated. The heat exchanger and gear pump are located outside the measurement cycle.

additional pressure sensor upstream of the cannula, the pressure sensor at the top of the reservoir can be validated to measure the pressure at the cannula entrance when the pump is directly mounted in the reservoir.

2.1.3 Numerical Setup

The software Simcenter STAR CCM+ (Siemens Digital Industries Software, USA) was used for the numerical investigation, and the calculations were executed on the Vienna Scientific Cluster (VSC). The following setup represents the baseline for the performed investigations. While structured grids are used for the spatial discretisation of the cannula and outlet draft, the grid of the volute and impeller are generated using polyhedral cells. An additional thin layer refinement guarantees

the desired cell distribution in the gaps between the housing and the impeller, see [2.3](#). The total number of cells is $\sim 12.9 \cdot 10^6$. The geometry was reconstructed based on a high-resolution Computed Tomography scan as described by Thamsen et al. [50](#). A mesh independence study, following the procedure outlined by Celik et al. [6](#), was performed. The resulting error estimates were $e_a^{21} = 1.78\%$, $e_{exp}^{21} = 1.46\%$, and $GCI_{fine}^{21} = 1.8\%$, with an apparent order of $p = 3.65$. The grid refinement ratios were $r_{21} = 1.25$ and $r_{32} = 1.31$.

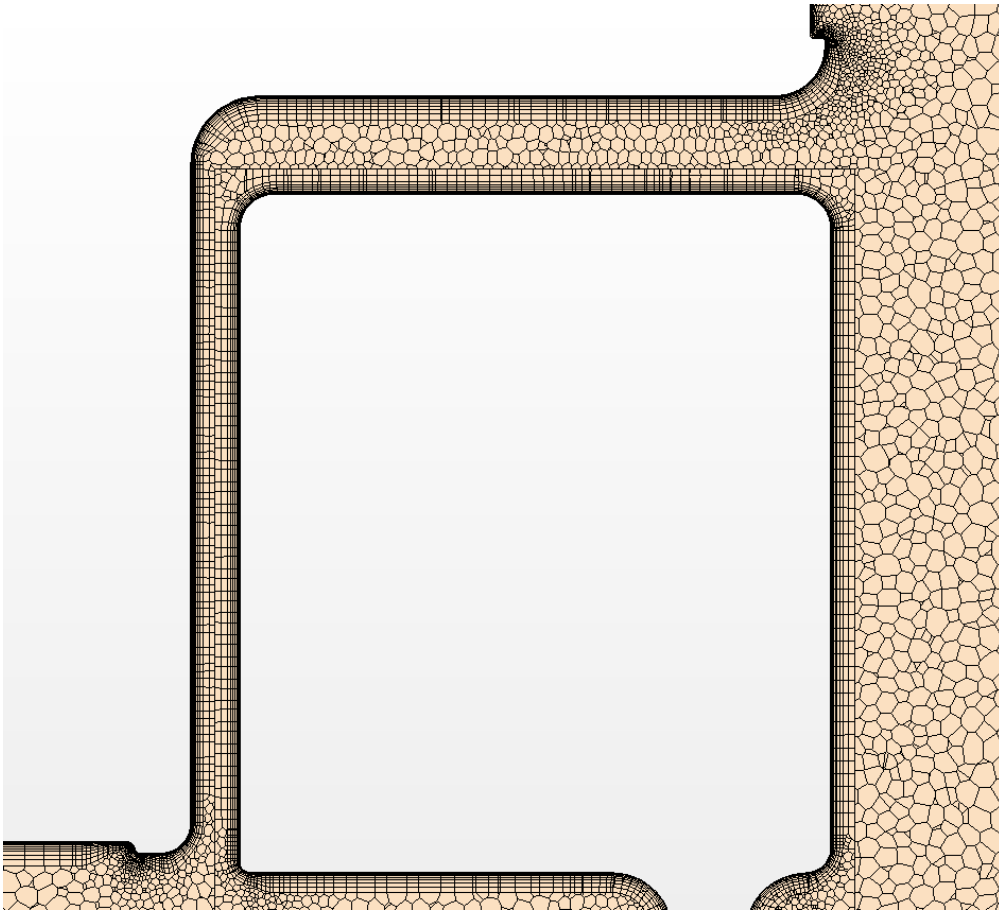


Figure 2.3: Thin mesh is used in the horizontal part of the top gap.

The same fluid properties as in the experiments were used, i.e. the density and viscosity are assumed to behave as constants. As turbulence is expected, the RANS equations are solved based on a segregated flow solver and turbulence is modelled with the $k - \omega$ SST model [32](#). The rotational motion of the impeller is implemented by the rigid body motion approach, commonly known as the sliding mesh approach. Therefore, the mesh of the moving domain (volume surrounding the impeller) is rotated every time step according to the rotational speed followed

by a re-meshing and interpolation at the interface. The time step is set equivalent to 4 *deg* rotation, resulting in $1.234 \cdot 10^{-4}$ s at 5400 *rpm*. Since the impeller moves, a transient solver is required. *Implicit Unsteady* is selected as it is more robust against large time steps than *PISO Unsteady*. A constant mass flow rate is defined as the inlet boundary condition for static conditions, and a constant pressure is set at the outlet. As an initial condition, the velocity and pressure field from a previous simulation is used [10]. The static investigations are performed mainly with a mass flow rate of 4.5 *l/min* and a speed of 5400 *rpm*. The convergence criterion requires that the residuals fall at least below $1 \cdot 10^{-4}$ and that the pattern of monitored flow quantities levels out over several rotations. The simulation duration includes at least 11 complete rotations, followed by averaging the results over the last three complete rotations. The surface-averaged static pressures are used to calculate the head pressure. Table 2.1 lists the simulations carried out for analysing numerical setup influences on the results for the static operation.

Table 2.1: Overview of static simulations

Investigation	Setup
Interface	3 different interfaces
Impeller position	axial and radial displacement
Turbulence	laminar vs. $k - \omega$ <i>SST</i> turbulence model
Motion	moving reference frame with mixing plane vs. sliding mesh

2.1.4 Investigation of Interfaces

As the bottom and top gap flow is crucial for predicting blood damage, a high flow resolution in these narrow regions is essential. Since numerical interpolation with potential errors is always needed at interfaces, their influence is investigated. Three different interfaces are designed; see Figure 2.4. The first interface, *IFgap*, is situated in the gap with stationary walls in relation to each domain. Secondly, an interface, *IFvolute*, including the top and bottom gap in the moving domain, is designed. With this approach, the enclosed housing walls are defined as stationary walls in relation to the global coordinate system, while the impeller wall moves with the moving domain. For the third design, the interface, *IFblade*, only includes the blade channel. Consequently, the remaining impeller walls excluded from the interface are defined as moving walls in relation to the global coordinate system.

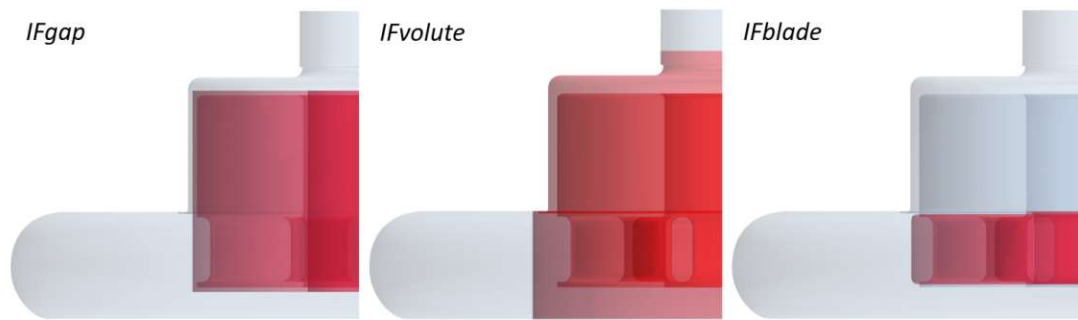


Figure 2.4: Designs of three investigated interfaces. The moving domain is highlighted in red.

2.1.5 Investigation of the Impeller Position

In the HM3, the impeller is electromagnetically levitated. Therefore, neither the axial nor the radial position is fixed but a result from the balance of forces (magnetic and hydraulic) acting on the impeller. Since the pressure distribution in the volute is not perfectly balanced, a radial and axial displacement due to the pressure distribution can be expected. In the numerical investigation, radial and axial displacement effects are analysed individually. Since experimental data was not available at that time, a radial displacement of $210 \mu\text{m}$ towards and away from the volute tongue and $500 \mu\text{m}$ towards the inlet cannula for the axial displacement was assumed.

2.1.6 Investigation of Turbulence

Previously, it was mentioned that turbulence is expected. The Reynolds number can be calculated to understand better if this expectation holds. The dimensionless Reynolds number is defined as the ratio of inertial to viscous forces and reads,

$$Re = \frac{uL}{\nu}, \quad (2.1)$$

where u is the velocity, L is the characteristic length and ν is the kinematic viscosity. At high Reynolds numbers, inertial forces dominate, and turbulence is likely to occur, while a low Reynolds number represents a laminar flow. For various applications, e.g. flow in a pipe, the regions for laminar ($Re < 2300$) and turbulent flow ($Re > 4000$) have been determined experimentally. Although such

regions do not exist for complex applications, e.g. centrifugal pumps, the flow in a pipe is a suitable approximation for the inflow through the inlet cannula. The velocity is calculated using the flow rate of 4.5 l/min and the cross-section at the inner diameter of the impeller, as this is the smallest. With the inner diameter as characteristic length and the kinematic viscosity, $\nu = \mu/\rho$, Re_I is 4500. At the beginning of the inlet cannula Re_C is 1600. It follows that the flow is in the transition regime, and neither a purely laminar nor a purely turbulent flow is expected. Therefore, two simulations were performed to compare the velocity fields obtained with the laminar governing equations.

2.1.7 Investigation of Motion Modelling

There are two approaches for simulating the rotation of the impeller or the mesh, respectively. In the first method, known as *sliding mesh*, the mesh of the moving domain is rotated by the desired angle at each time step. In this method interpolation at the interface after each time step is necessary. To avoid this, the mesh in the *moving reference frame* method stays constant while an additional source term is added in the governing equations. Since the position of the impeller is frozen in this analysis, the flow depends on the relative position of the impeller. To overcome this dependence, the *mixing plane* analysis is used. Thereby, the flow is averaged circumferentially on both sides of the interface and applied for all interface mesh cells. While the *mixing plane* methodology can be expected to produce reasonable global results, it cannot resolve the unsteady flow field due to the impeller rotation, as the sliding mesh is capable of.

2.1.8 Investigation of Roughness

The potentially positive effects of roughness on thrombogenicity, as described in Section 1.2, may also be accompanied by a reduction in hydraulic efficiency [53]. The microspheres have a diameter of approximately $100 \mu\text{m}$, forming a roughness of $Ra = 15 \mu\text{m}$ or $Rz = 90 \mu\text{m}$, respectively [22]. The effect of rough walls is either taken into account by correcting the wall function via the roughness function based on empirical parameters or by resolving the rough structure in the mesh. Since resolving the structure is associated with high computational costs and requires a correspondingly fine mesh, using wall functions is the more suitable approach. The

wall function itself is an empirical model of the dimensionless velocity u^+ , which is divided into the viscous sublayer for $y^+ < 5$, the logarithmic layer for $y^+ > 30$, and the buffer layer in between. The dimensionless wall distance is given by

$$y^+ = \frac{yu^*}{\nu}, \quad (2.2)$$

where y is the actual distance to the wall, u^* is the shear velocity, and ν is the kinematic viscosity. The wall function in the following form is called the blended wall function and is derived from the law of the wall,

$$u^+ = \frac{1}{\kappa}(1 + \kappa y^+) + C \left(1 - e^{y^+/y_m^+} - \frac{y^+}{y_m^+} e^{-by^+} \right), \quad (2.3)$$

where

$$C = \frac{1}{\kappa} \ln \left(\frac{E'}{\kappa} \right), \quad (2.4)$$

$$b = \frac{1}{2} \left(y_m^+ \frac{\kappa}{C} + \frac{1}{y_m^+} \right), \quad (2.5)$$

$$E' = \frac{E}{f} \quad (2.6)$$

and κ is the von Karman constant, E is the log law offset, and f_r is the roughness function [40]. To formulate the roughness function, a dimensionless roughness parameter, analogous to equation [2.2], is introduced

$$R^+ = \frac{ru^*}{\nu}, \quad (2.7)$$

where r is the equivalent sand grain roughness. Since the coating consists of microspheres, which already represent sand grains, their diameter can be used for the equivalent sand grain roughness. The roughness function is expressed as a function of the roughness parameter R^+

$$f_r = \begin{cases} 1 & \text{for } R^+ \leq R_{smooth}^+ \\ \left(B \left(\frac{R^+ - R_{smooth}^+}{R_{rough}^+ - R_{smooth}^+} \right) + CR^+ \right)^a & \text{for } R_{smooth}^+ < R^+ \leq R_{rough}^+ \\ B + CR^+ & \text{for } R^+ > R_{rough}^+ \end{cases}, \quad (2.8)$$

where

$$a = \sin \left(\frac{\pi}{2} \frac{\log(R^+/R_{smooth}^+)}{\log(R_{rough}^+/R_{smooth}^+)} \right) \quad (2.9)$$

and the empirical model coefficients B , C , R_{smooth}^+ and R_{rough}^+ [45]. Figure 2.5 shows the corrected wall function for various roughness parameters. The increasing roughness causes a downward shift of the logarithmic layer as it changes the log law offset E in equations 2.3-2.6.

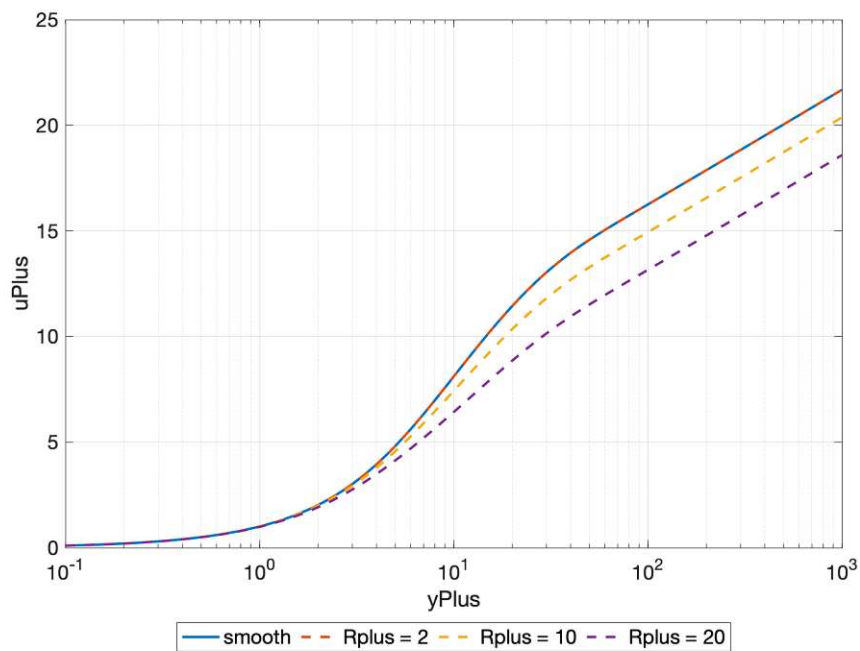


Figure 2.5: Shift of the wall function in the logarithmic layer for various roughness parameters.

2.2 Results

2.2.1 Experimental Results

The static characteristics of the two experimental setups, *modVolute* and *modInlet*, in Figure 2.6 show a good overall agreement. The measured head pressure is calculated with the pressure measured in the left ventricular reservoir for the *modVolute* setup, the pressure measured in front of the cannula in the *modInlet*

setup and the pressure measured directly after the outlet for both setups. The deviation peaks between 3 and 6 l/min , increasing with the speed of the impeller. Assuming that the deviation due to roughness is constant over the flow rate as reported by Wang et al. [53] and Torner et al. [51], the peaks are not attributable to roughness effects. In the *modInlet* setup the relative error between the pressure sensor in the left ventricular reservoir and 1 cm upstream of the cannula is below 1.3 %; see Figure 2.7.

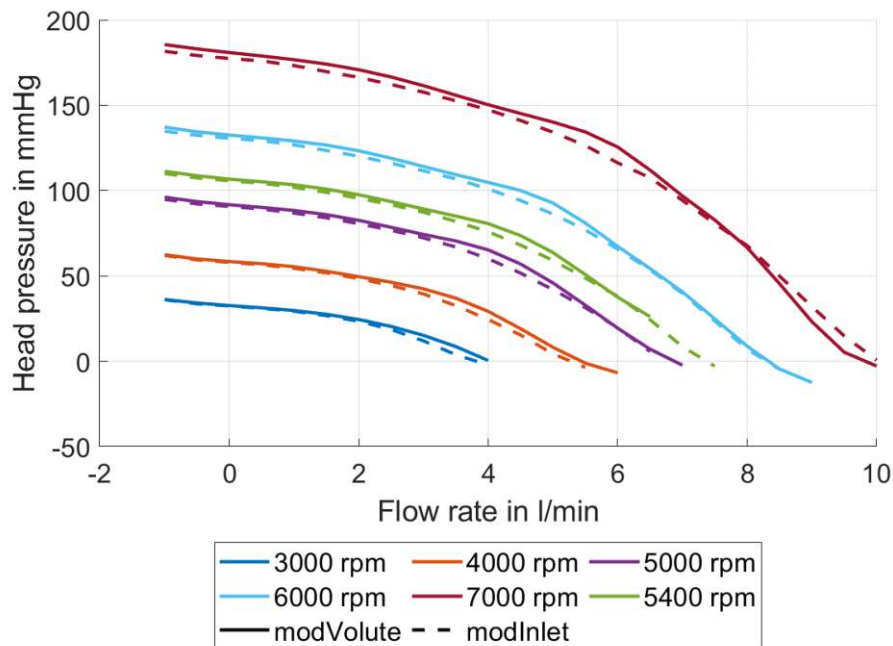


Figure 2.6: Static characteristics of the two experimental setups, *modVolute* and *modInlet*, show overall good agreement, although peaks occur in the medium flow rate range.

2.2.2 Investigation of Interfaces

Although there is no deviation from the calculated pressure head (IF_{gap} : 82.30 $mmHg$, IF_{volute} : 82.95 $mmHg$, IF_{blade} : 82.58 $mmHg$), differences can be observed with regard to numerical fluctuations and the flow in the top gap. For the interface IF_{blade} , strong numerical fluctuations in the computed head pressure occur as shown in Figure 2.8.

Despite applying a thin mesh, the number of cells in the top gap is small. Since

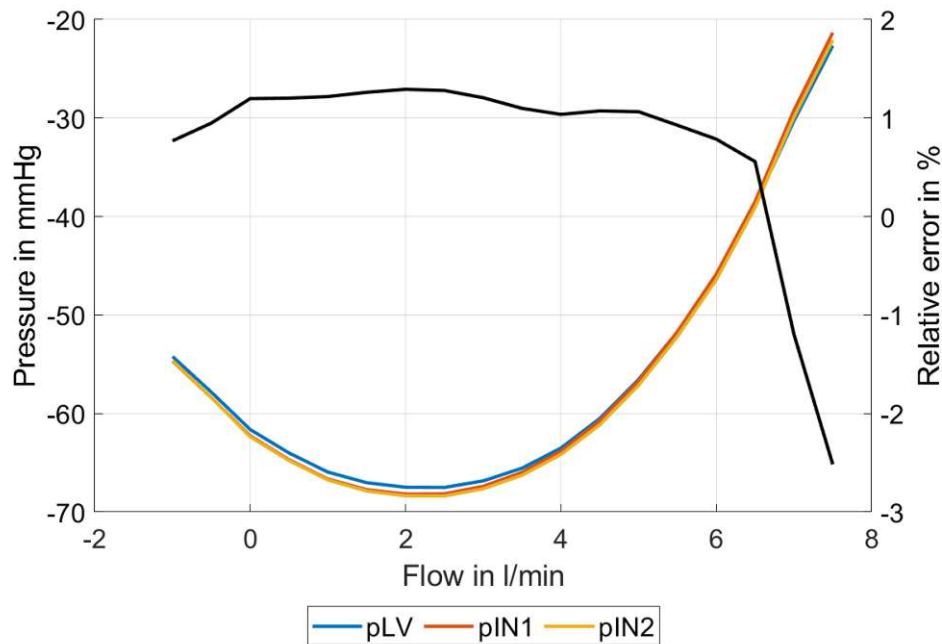


Figure 2.7: Pressures measured in the left ventricular reservoir p_{LV} , 15cm in front of the cannula p_{IN1} , 1 cm in front of the cannula p_{IN2} , along with relative error between p_{IN2} and p_{LV} .

the interface IF_{gap} is located in the gap, a high dependence on the number of cells is observed to achieve a reasonable resolution of the Taylor vortices.

Taylor vortices are observed between the two concentric cylinders for all three types of interfaces. As illustrated in Figure [2.9](#), the Taylor vortices using the interface IF_{gap} have a less pronounced upwards drift.

2.2.3 Investigation of the Impeller Position

The resulting head pressures are 82.1 mmHg for the radial displacement towards the tongue, 82.1 mmHg for the radial displacement away from the tongue, and 81.5 mmHg for axial displacement.

The predicted secondary mass flows for the investigated impeller displacements are listed in Table [2.2](#). Although smaller shifts of the mass flow rate between the top and bottom gap are observed, the overall secondary flow rates do not change.

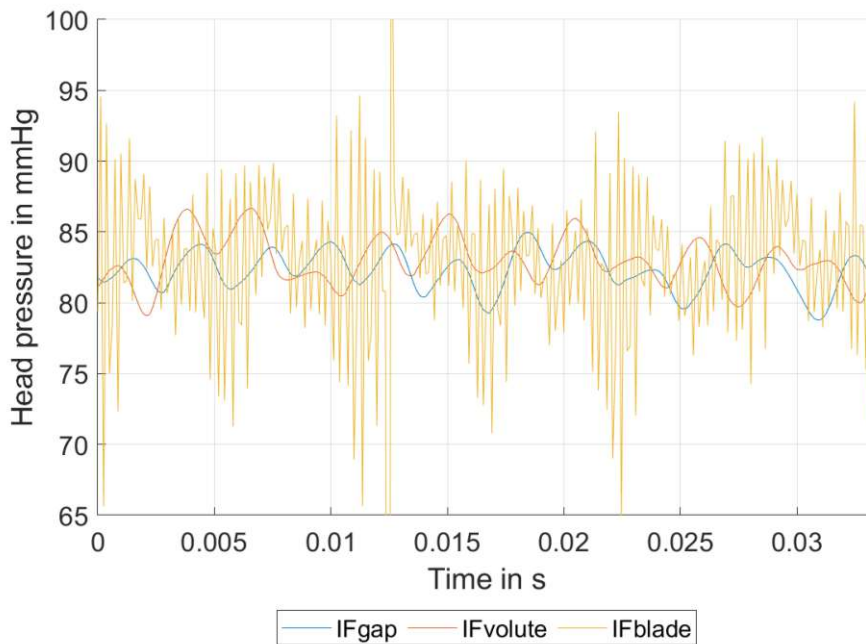


Figure 2.8: Head pressures using the interfaces *IFgap* and *IFvolute* resolve the fluctuations caused by the impeller blades bypassing, while numerical oscillations occur when using the *IFblade* interface.

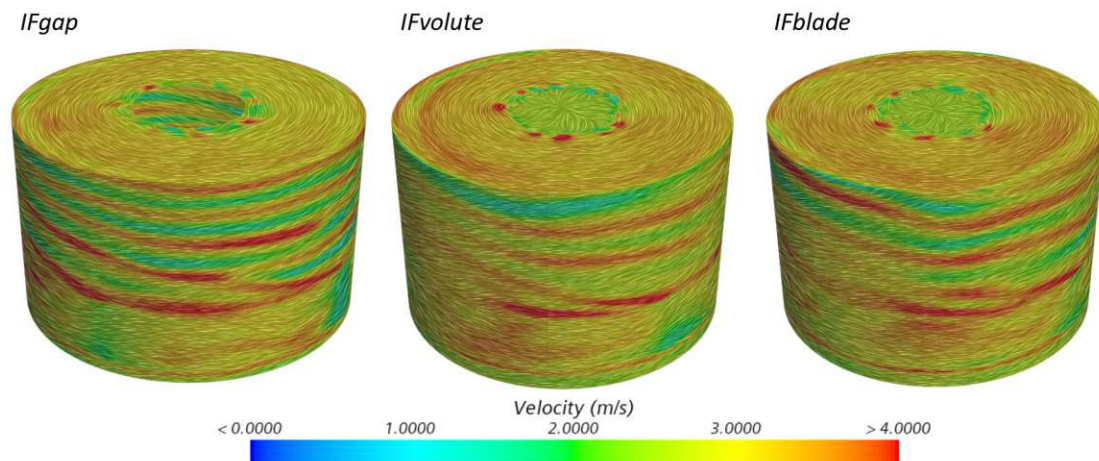


Figure 2.9: Velocity fields at the centre of the gap for each interface show good agreement, although the Taylor vortices have a less pronounced upward drift when using the *IFgap* interface.

2.2.4 Investigation of Turbulence

The head pressures agree for both setups (laminar: 82.80 *mmHg*, turbulent: 82.53 *mmHg*). As marked in Figure [2.10](#), the laminar flow separates earlier from

Table 2.2: Predicted mass flow due to impeller displacement, where Q_{total} is volume flow rate through blade channel, Q_{top} through top gap and Q_{bottom} through bottom gap in l/min .

	no disp.	radial towards tongue	radial away from tongue	axial
Q_{total}	5.73	5.73	5.73	5.73
Q_{top}	0.56	0.59	0.62	0.54
Q_{bottom}	0.64	0.66	0.63	0.7
Q_{top}/Q_{total}	0.10	0.10	0.11	0.10
Q_{bottom}/Q_{total}	0.11	0.12	0.11	0.12
$(Q_{top} + Q_{bottom})/Q_{total}$	0.21	0.22	0.22	0.22

the blades.

2.2.5 Investigation of Motion Modelling

Although the calculated head pressures agree for both methods, the *moving reference frame* method is not capable of resolving the pressure fluctuation due to the bypassing of the blades as shown in Figure 2.11. The averaging of the flow field can be seen in Figure 2.12. Due to the averaging using *moving reference frame*, the flow near the interface is more uniform. However, the main flow characteristics in the blade channel remain comparable. Since the top gap entrance is close to the interface and the flow at the entrance is more uniform, the Taylor vortices separate more clearly, as depicted in Figure 2.13.

2.2.6 Investigation of Roughness

The roughness parameter R^+ for the investigated operating point is illustrated in Figure 2.14. Apart from the tongue ($R^+ \approx 20$) and the bottom gap ($10 < R^+ < 20$), the roughness parameter is below 10. Since the wall function represents

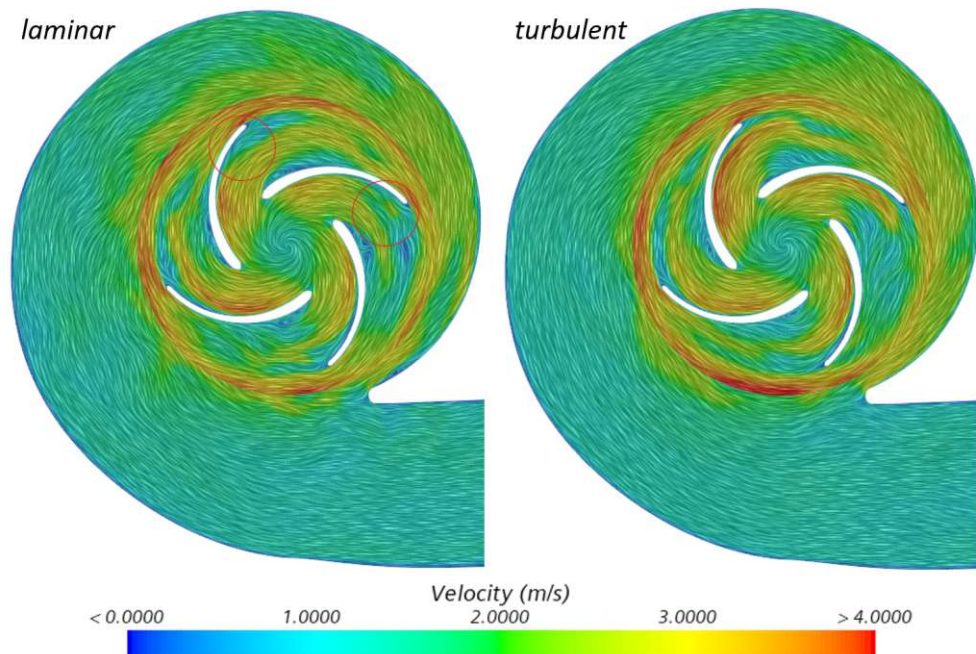


Figure 2.10: Relative velocity fields at horizontal plane at the centre of the blade channel solving laminar and turbulent equations. Earlier separation from the blades compared to turbulent flow is marked. At 4.5 l/min and 5400 rpm , using *sliding mesh* method.

a model for the first cell on the wall, a correspondingly large cell ($y^+ > 10$) is required to take the roughness effect into account. This would result in a coarse mesh that would not be able to properly resolve the flow in the area of the tongue. However, given that the overall influence for the existing R^+ values is small, as shown in Figure [2.5](#), the roughness can be neglected in numerical investigations.

2.2.7 Comparison of the Experimental and Simulated Results

The comparison of the measured and predicted head pressures is performed for three operating points at flow rates of 2.5 , 4.5 , and 6.5 l/min and 5400 rpm . The measured data from the *modVolute* setup are used. All examined points exhibit a comparable total deviation of less than 10 mmHg , as listed in Table [2.3](#). Figure [2.15](#) compares the predicted head pressures with the measured characteristic curve.

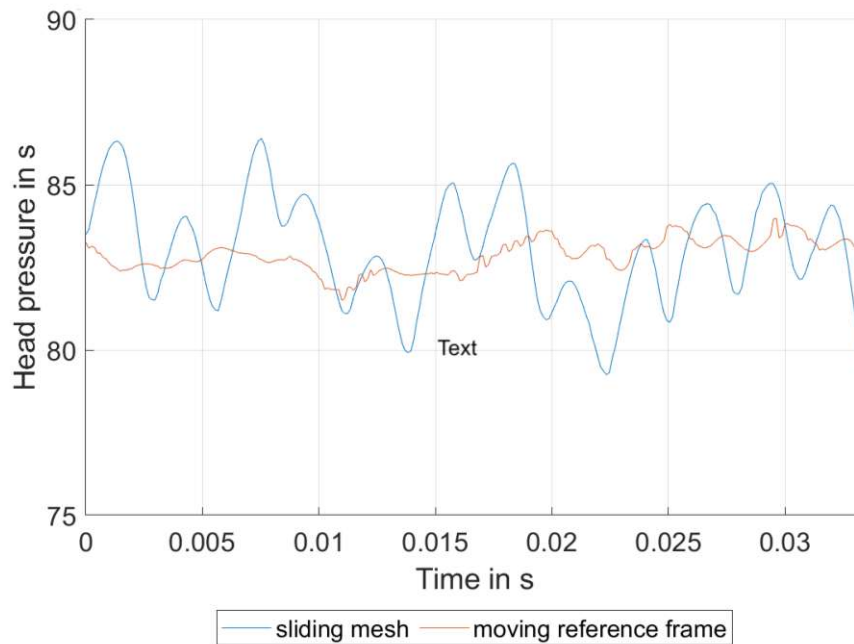


Figure 2.11: Head pressures over time using the *sliding mesh* and *moving reference frame* methods have comparable means, but the pressure fluctuations caused by blade bypassing are not resolved with the *moving reference frame* method.

Table 2.3: Measured versus predicted head pressures.

Flow rate in l/min , head pressures in $mmHg$.

Flow Rate	Measured Head Pressure	Predicted Head Pressure	Deviation
2.5	93.6	101.2	7.6
4.5	73.6	82.7	9.1
6.5	26.2	33.8	7.6

2.3 Discussion

To identify the reason for the deviation between measured and predicted results, one *in-vitro* and five *in-silico* settings have been investigated. The overall good agreement of the measured results using the two setups, *modVolute* and *modInlet*, leads to the conclusion that mounting the pump directly in the reservoir has no significant influence on the pump performance. However, the peak value at the

Simcenter STAR-CCM+

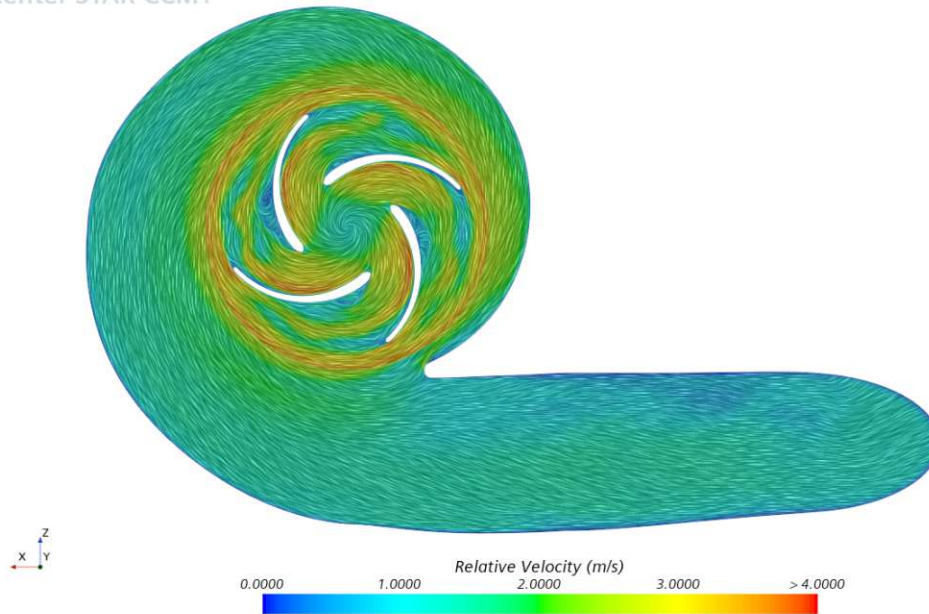


Figure 2.12: Relative velocity field at the horizontal plane at the centre of the blade channel. 4.5 l/min at 5400 rpm, using the *moving reference frame* method. The circumferential averaging is clearly visible.

middle range of the flow rate, depicted in Figure [2.6](#), may be related to the inlet conditions or the reservoir, respectively.

Furthermore, the pressure measurement at the top of the reservoir correctly represents the pressure in front of the cannula, as demonstrated with the *modInlet* setup. Together with the numerical investigations of roughness, the experiments do not indicate any roughness effects.

Due to the lack of a commonly known standard for setting the interface between stationary and moving domains, three options have been tested. While the interface in the gap introduces interpolation in a critical area, the interface, including only the blade channel, has an insufficient distance to the blade tips, which is a potential cause of the observed numerical fluctuations. Placing the interface in the volute not only avoids these issues but also allows the use of *mixing plane* averaging. This option is unavailable for the interface in the gap, as it would average out the Taylor vortices.

Although it has been shown that using *moving reference frame* motion modelling in combination with *mixing plane* averaging can predict global parameters, local

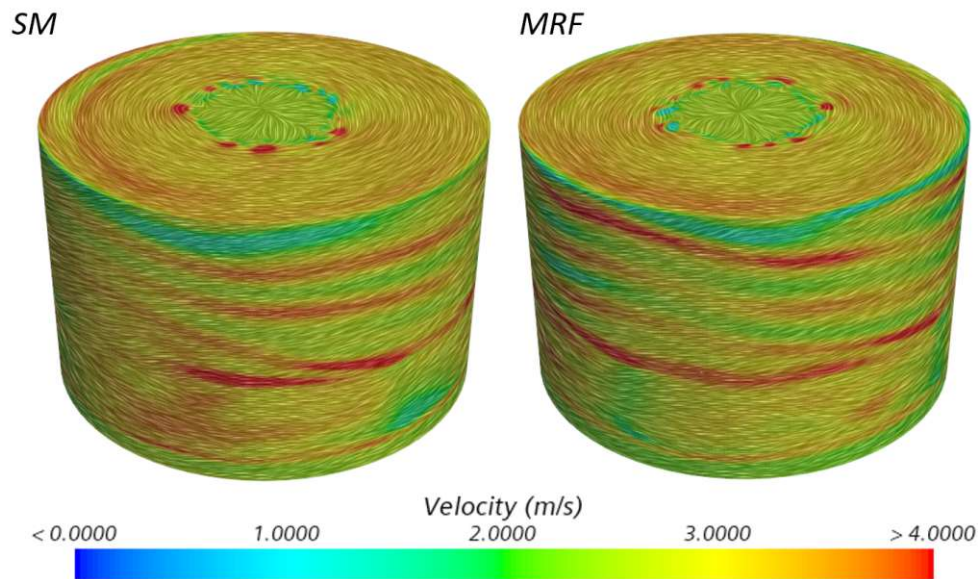


Figure 2.13: Velocity fields at the centre of the top gap at 4.5 l/min and 5400 rpm, using the *sliding mesh* and *moving reference frame* methods. The *mixing plane* averaging results in a clearer separation of the Taylor vortices when using the *moving reference frame* method.

flow phenomena due to the bypassing of the impeller blades are no longer resolved. Furthermore, the development of the Taylor vortices in the top gap is also influenced. Nevertheless, this option enables further investigations to reduce computational costs.

In previous literature, both laminar [4] and turbulent flow [11, 54] have been assumed. This work has shown that modelling turbulence at the investigated operating point is unnecessary when predicting global parameters. However, since the pump operates in the transition range, this statement does not necessarily apply at higher speeds or higher mass flows, respectively. Furthermore, detailed, local investigations of the shear rates in the blade channels are required to estimate the effect of the different flow separations on hemolysis.

The investigation of the impeller position indicates a shift of the secondary flow rates from the top to the bottom gap and vice versa but does not affect the global performance. The deviation between measured and predicted results is comparable in the total amount with a peak in the middle of the flow rate range, leading to the question of how to quantify the error, as a relative consideration would increase the error drastically at low head pressures or high mass flows, respectively.

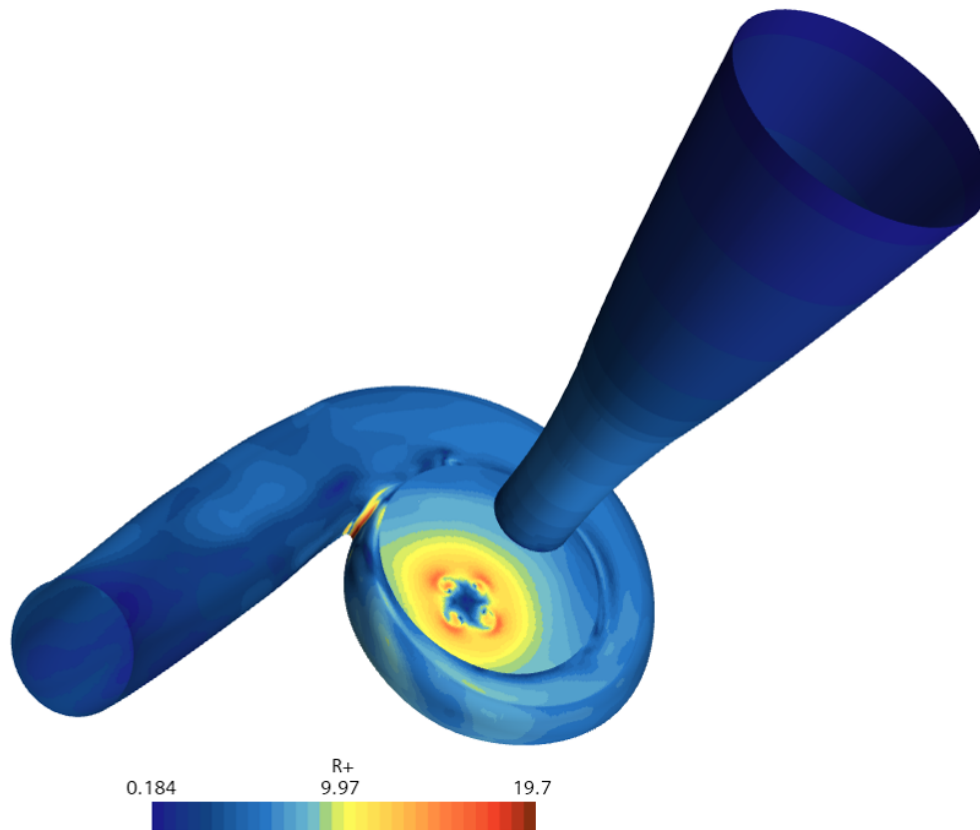


Figure 2.14: Roughness parameters derived from Simcenter STAR CCM+ show values above 10 in the bottom gap and the tongue region.

Possible reasons for the inadequate performance of the pump compared to the predicted performance may include deviations in the geometry, accompanied by part-load losses, such as recirculations [16].

2.4 Conclusion

This investigation focused on the numerical setup to create a benchmark for static simulations of the HM3 using the same fluid properties as in the experiment. The reason for the deviation between the measured and predicted head pressure could not be found. However, questions regarding the interface's position, turbulence modelling, and roughness could be clarified. Furthermore, the influence of impeller displacement in static operation could be excluded. Although suction directly out of the reservoir potentially influences a short operation range, the overall performance

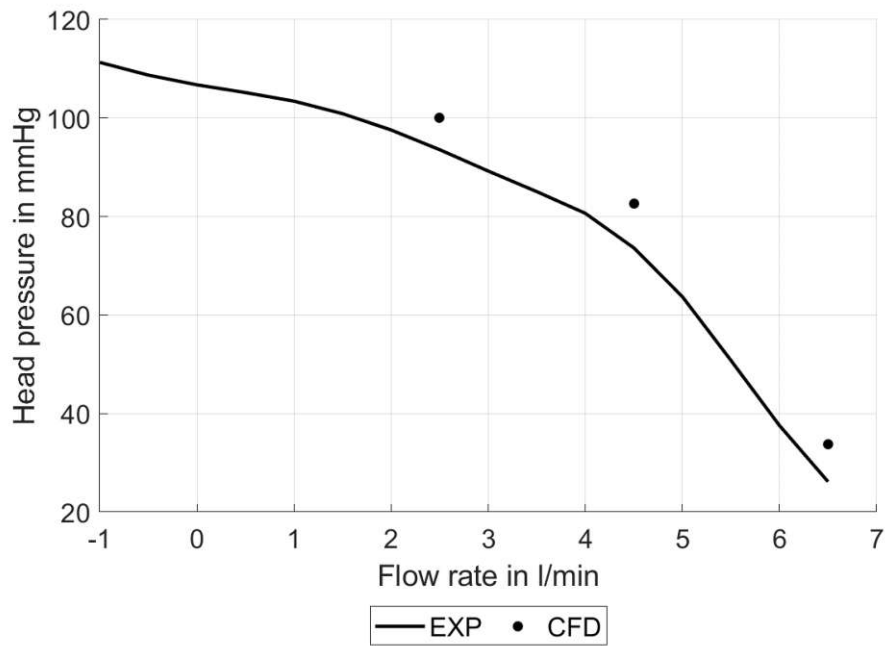


Figure 2.15: Measured versus predicted head pressure at 2.5, 4.5 and 6.5 l/min and 5400 rpm using the *modVolute* setup.

is unaffected. Further, experimental investigations in search of unrecognised losses are necessary. The investigation of local flow phenomena may lead to an explanation.

Chapter 3

Objective 2 - Dynamic Investigation

Establishing a numerical flow simulation methodology and benchmark solutions for the HM3 rotodynamic blood pump at dynamic operating conditions by validating experiments using the same fluid properties.

3.1 Method

3.1.1 Experimental Setup

The mock loop described in [2.1.1](#) allows the control of the pressure in the two reservoirs, namely the left ventricular and the aortic reservoirs. It is, therefore, possible to mimic the cardiac cycle of specific patients. The dynamic properties of the pump can be described by measuring the pressure in the left ventricular reservoir, which represents the inlet pressure and is directly downstream of the pump outlet, as well as the associated volume flow.

Several cardiac cycles are measured at an impeller speed of 5400 *rpm*, then divided into individual cardiac cycles and averaged over the total number of cycles. In this way, the head pressure and the volume flow of a cardiac cycle are obtained. This procedure is carried out for both setups, i.e. *modVolute* and *modInlet*.

With the *modVolute* setup, the impeller speed is additionally measured via a

mounted hall sensor, as the controller of the HM3 only estimates the speed. As the volume flow rate depends mainly on the speed of the impeller, fluctuations in speed directly affect the results.

As a moving mass has the potential to influence the dynamic behaviour, a deeper understanding of the impeller movement is required. Therefore, the radial and axial displacements are measured as well. While the HM3 controller estimates the radial displacement, the axial displacement is measured optically via a laser distant meter.

3.1.2 Numerical Setup

Based on the previous chapter, the numerical investigations are examined using the interface *IFvolute* with the same mesh. Roughness and impeller displacement are neglected.

The measured and averaged mass flow, representing the cardiac cycle, is used as the boundary condition, while a reference pressure is defined at the opposite boundary. This is possible because only the pressure difference compared to the reference pressure is of interest with incompressible fluids. Two simulations are performed since fixing the pressure at the boundary may not accurately represent the physics in dynamic applications. In the first simulation, the pressure reference is defined at the outlet, while in the second, it is defined at the inlet boundary condition.

Due to the temporarily higher flow rate compared to the static operation examined in Section 2.1.6, the Reynolds number is also higher. Consequently, the effect of modelling turbulence is analyzed numerically. As listed in Table 1.2, the $k-\omega$ SST model is most commonly used and therefore compared in this study to the laminar case.

Building on the promising results of the *moving reference frame* method for static applications (see Section 2.2.5), its performance is also investigated under dynamic conditions and compared to the *sliding mesh* method. For the *moving reference frame*, not only the *mixing plane* method but also the *frozen rotor* method in two different rotor positions is applied, as it has been used in the literature (see Table 1.2).

The simulations are performed using the time-varying boundary conditions from

both test setups. Thereby, the potential effects of the inlet environment on the time-varying dynamic boundary condition can be investigated.

In addition to the mesh independence performed in Chapter 2, a time-step study has been conducted.

Table 3.1 lists the investigations carried out.

Table 3.1: Overview of dynamic simulations

Investigation	Setup
Boundary condition	mass flow as inlet vs outlet BC
Turbulence	laminar vs. $k - \omega$ <i>SST</i> turbulence model
Motion	mixing plane vs. frozen rotor vs. sliding mesh
Inlet Environment	BC from <i>modVolute</i> and <i>modInlet</i>
Time step	4-72 degrees for mixing plane and 4-16 degrees for sliding mesh

3.2 Results

3.2.1 Experimental Results

The analyzed cardiac cycles are displayed in Figure 3.1 on the left side for the *modVolute* setup and on the right side for the *modInlet* setups. The numbers of detected cardiac cycles are 40 for *modVolute* and 39 for *modInlet*. All detected cardiac cycles match well without any outliers.

The averaged head pressure and flow rate are presented in Figure 3.2. Since the pressure is controlled in the reservoirs, but the head pressure is calculated using the left ventricle pressure sensor for *modVolute* and the additional pressure sensor mounted in front of the cannula for *modInlet*, the resulting cardiac cycles differ.

First, pressure oscillations occur with the extreme values for *modInlet*. Such oscillations are filtered out for *modVolute* due to the mass of the fluid in the reservoir and the air at the top of the reservoir, where the pressure sensor is mounted. In addition, *modVolute* exhibits a higher rate of pressure change due to less damping as no tube in front of the cannula is added. While the mass flow for *modInlet* shows a uniform rise and fall, the mass flow for *modVolute* increases

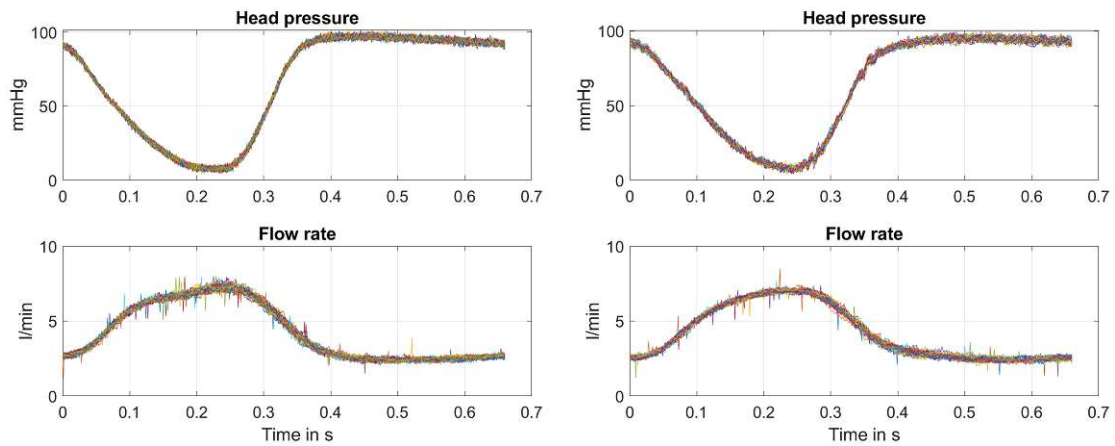


Figure 3.1: Detected cardiac cycles at 5400 rpm using the *modVolute* setup on the left side and the *modInlet* setup on the right side.

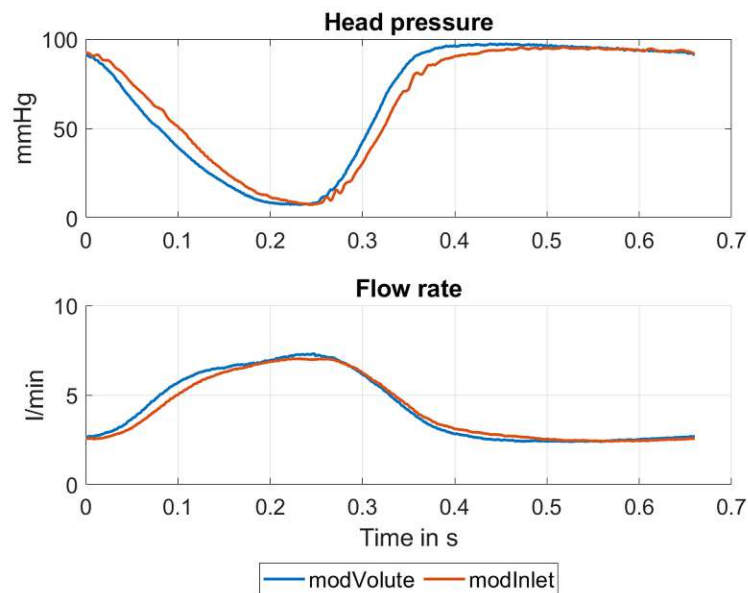


Figure 3.2: Averaged cardiac cycles at 5400 rpm for the *modVolute* and *modInlet* setups show that head pressure changes more rapidly in the *modVolute* setup. An additional increase in flow rate between 0.2 s and 0.28 s is also observable for the *modVolute* setup.

between 0.2s and 0.28s. Although the head pressures during systole result in the same minimum, the corresponding flow rate is higher for *modVolute*.

The additional data measured with the *modVolute* setup are outlined in Figure 3.3 on the left side. The fluctuation of the impeller speed is below 1.2%. While

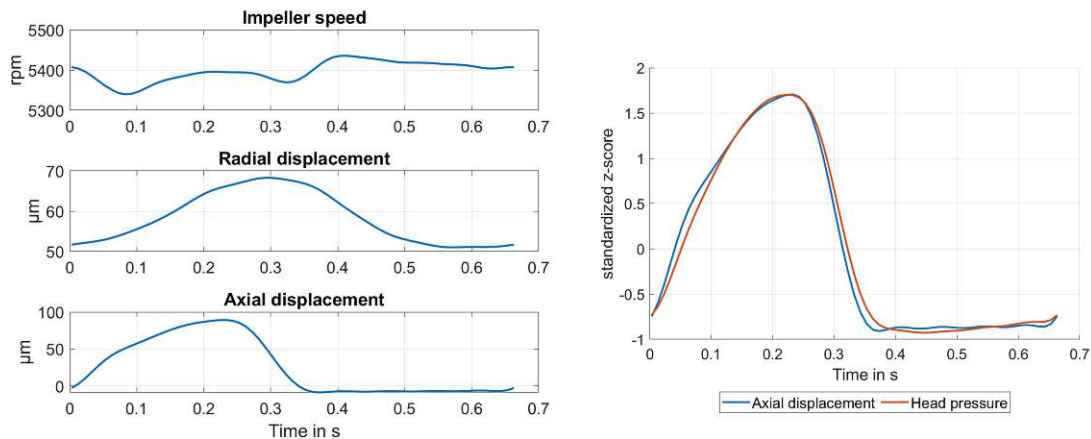


Figure 3.3: Additionally measured data of the averaged cardiac cycle at 5400 rpm for the *modVolute* setup. The left figure depicts the correlation between axial displacement and inverse head pressure at 5400 rpm.

axial displacement shows an inverse relationship with head pressure, as depicted in Figure 3.3 on the right side, no significant correlation is observed for radial displacement, even though the pattern repeats with the cardiac cycle. Additionally, the HM3 does not provide any information regarding the direction of the radial displacement.

3.2.2 Investigation of Boundary Condition

Figure 3.4 presents the head pressure and the pressure at the cannula inlet and pump outlet. The fixation of the pressure due to the reference pressure boundary condition is clearly visible. Although the resulting head pressure is comparable, the fluctuation due to bypassing the pressure blades develops either upstream towards the inlet or downstream towards the outlet. While the effect on the global performance is negligible, there is an influence on the local flow.

3.2.3 Investigation of Turbulence

Figure 3.5 presents the predicted head pressures. Similar to the static results presented in Section 2.1.6, the head pressure agrees with lower flow rates. For higher flow rates, which occur at low head pressures, the relative error increases to 23%, while the absolute error increases only slightly and remains under 3 *mmHg*

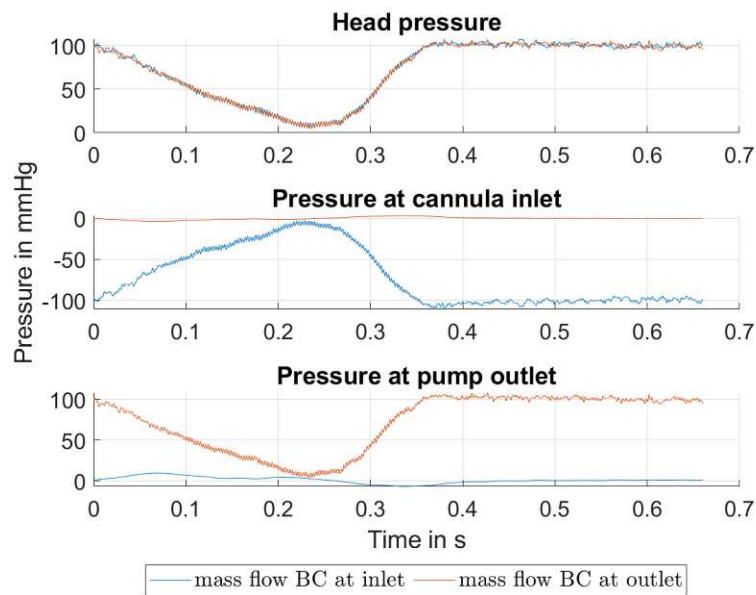


Figure 3.4: Predicted pressures when applying the time-varying mass flow boundary condition at the inlet and outlet. Fluctuations can be observed either upstream or downstream of the flow, depending on the fixed reference pressure boundary condition.

with an RMSE of 1.6 mmHg . Hence, turbulence starts to occur with higher flow rates of the analyzed cardiac cycle.

3.2.4 Investigation of Motion

The results of the various motion modelling methods are illustrated in Figure [3.6](#). The two simulations using the *frozen rotor* method differ significantly, particularly at high head pressures. Consequently, the *frozen rotor* method fails to predict reasonable results. Similar to the static investigations carried out in Section [2.2.5](#), the *mixing plane* method performs well with an RMSE of less than 1 mmHg , a maximum absolute error of less than 3 mmHg and a relative error of less than 13% compared to the results using *sliding mesh* method.

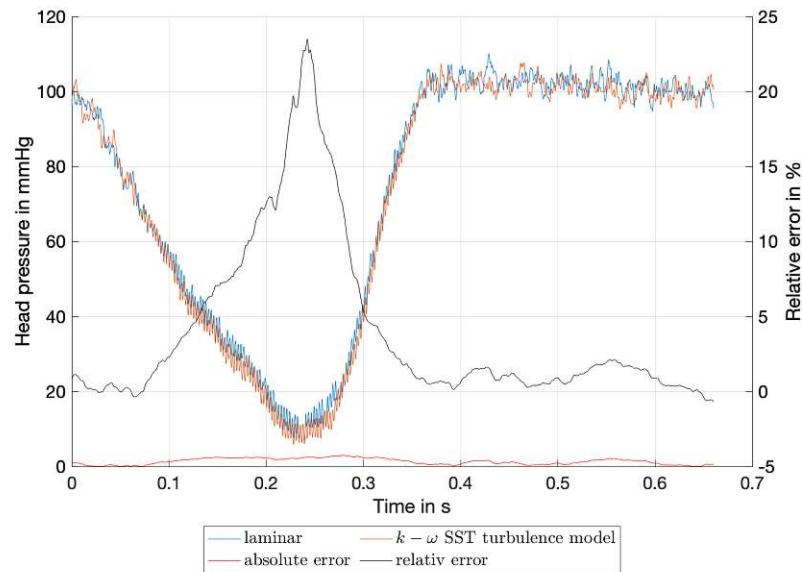


Figure 3.5: Predicted head pressures using laminar and turbulent models show overall good agreement, although deviations start to occur with higher flow rates as turbulence emerges.

3.2.5 Investigation of Speed Fluctuations

As depicted in Figure 3.7, no significant deviation is detected when the rotational speed fluctuation is considered. This is to be expected, as the measured fluctuation is below 1.2%.

3.2.6 Investigation of Time Steps

Various time steps between 4 degrees ($\simeq 1.2 \cdot 10^{-4}$ s) and 72 degree ($\simeq 2.2 \cdot 10^{-3}$ s) per step have been investigated for *moving reference frame* in combination with *mixing plane*. Starting with 72 degrees, a deviation, especially in high flow regions, is visible (see Figure 3.8). With *sliding mesh*, the highest investigated time step is 16 degrees ($\simeq 4.9 \cdot 10^{-4}$ s), as the fluctuation in pressure due to bypassing of the impeller blades is no longer resolved, as depicted in Figure 3.8, and therefore the use of *sliding mesh* is no longer beneficial.

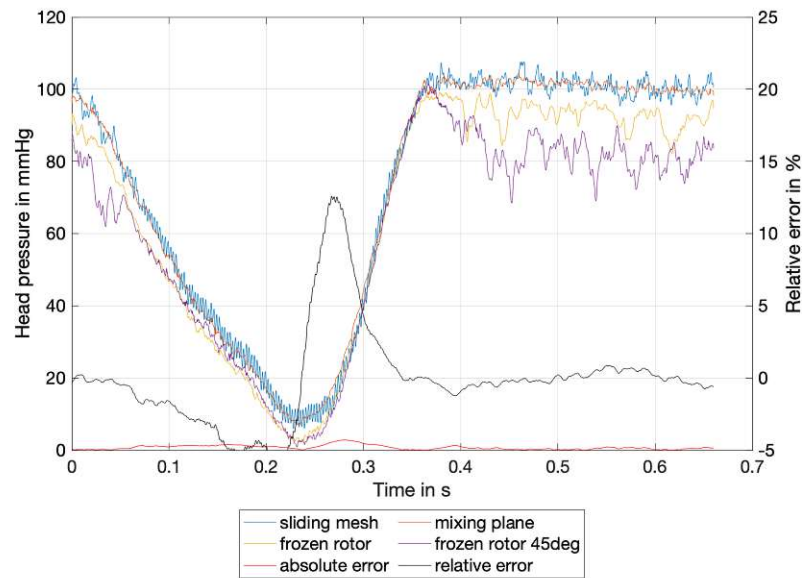


Figure 3.6: Predicted head pressures using the *sliding mesh*, *mixing plane*, and *frozen rotor* methods. Absolute and relative errors are outlined for *mixing plane* vs. *sliding mesh*. The *frozen rotor* approach fails to accurately predict the head pressure, whereas the *mixing plane* method performs well.

3.2.7 Comparison of Experimental and Numerical Results

The comparison between experimental and predicted head pressures is illustrated in Figure 3.9 for the *modVolute* setup and in Figure 3.10 for the *modInlet* setup. The predicted pressure is shifted to fit the end-diastolic head pressure to exclude estimated static errors.

To quantify the deviation, the relative and absolute RMSE of the head pressure, as well as the ratio of the enclosed area in the HQ diagram (see Figures 3.9 and 3.10), are calculated and listed in Table 3.2. The shifted head pressure is used for both RMSE and averaged over time; otherwise, the pressure fluctuation due to the bypassing of the impeller blades would generate additional errors.

There are several differences in the characteristic loop in the HQ diagram between the two experimental setups:

First, the predicted loop for *modVolute* shows no widening in the end-systolic phase and reaches a lower head pressure than measured. In contrast, the end-systolic and

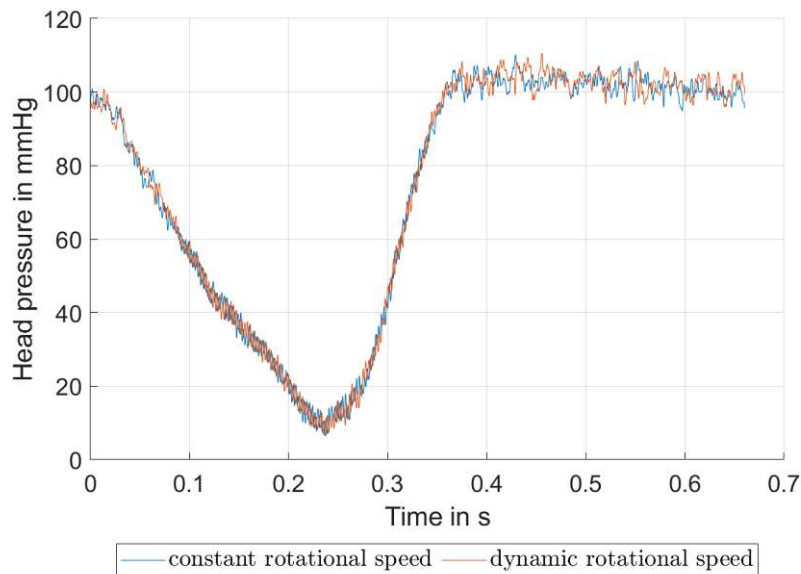


Figure 3.7: Predicted head pressures using constant impeller speed and measured impeller speed show no significant deviation.

Table 3.2: Predicted vs. experimental results

	Relative RMSE	Absolute RMSE	Ratio of area
<i>modVolute</i>	1.06	4.88	0.44
<i>modInlet</i>	1.09	3.98	0.85

end-diastolic head pressures for the *modInlet* setup align.

Additionally, a crossing of the predicted loop is observed for both setups, though it is more pronounced in the *modVolute* setup.

Finally, while the diastolic phase in the *modVolute* setup aligns well, the predicted loop follows a narrower trajectory during systole. In the *modInlet* setup, both phases initially match well, but the predicted loop narrows at the end of systole and widens at the end of diastole.

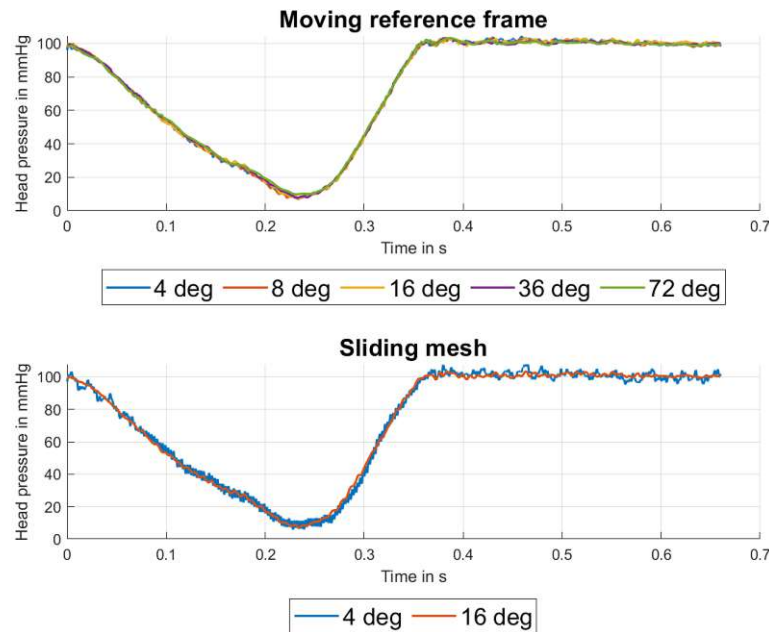


Figure 3.8: Predicted head pressure for different time steps using *moving reference frame* in combination with *mixing plane* at the top and *sliding mesh* at the bottom. With a time step of 72 degrees, the results using *moving reference frame* method start to deviate. Starting with 16 degrees, the pressure fluctuations caused by the bypassing of the impeller blades are no longer resolved when using the *sliding mesh* method.

3.3 Discussion

3.3.1 Experimental Results

The difference in head pressure between the two setups can be explained by the additional fluid inertia introduced by the mounted inlet tube. In Figure [3.11](#), the head pressures calculated with the pressure sensors in the reservoir, 15 cm and 1 cm in front of the cannula, and the same outlet pressure are outlined. The effect of additional fluid inertia is evident when examining Equation [1.15](#). Given that the flow change is uniform across all measurement points, an increased inertia constant corresponds to a greater change in head. Consequently, the greatest change in head pressure is observed in the measurement corresponding to the pressure in the reservoir.

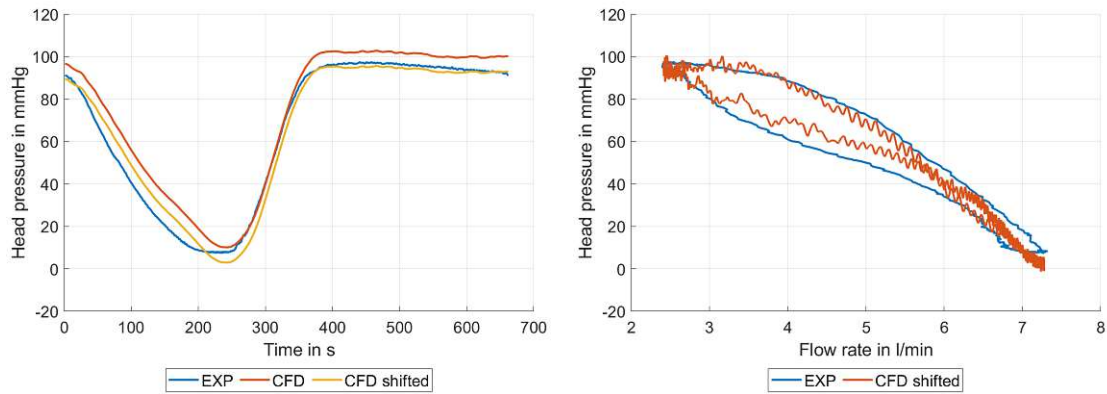


Figure 3.9: Experimental versus predicted head pressure over time on the left side and overflow on the right side, using the *modVolute* setup. Numerical results are additionally corrected to exclude estimated static errors.

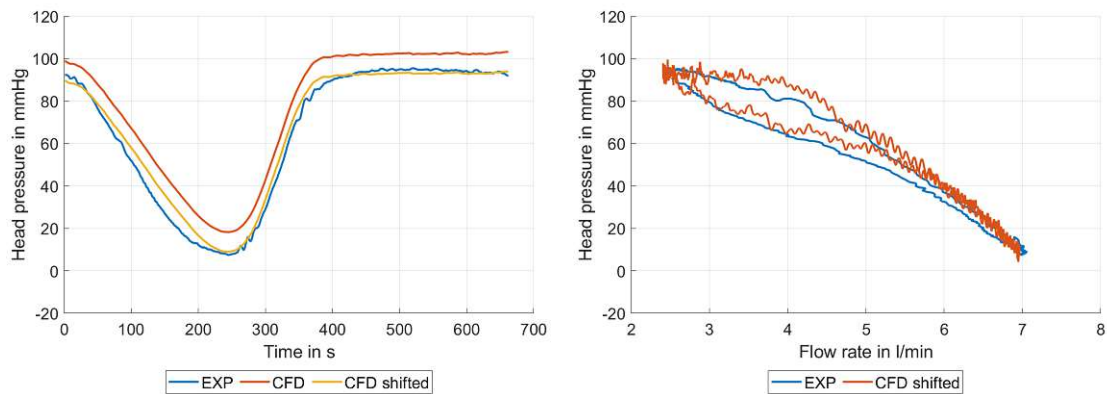


Figure 3.10: Experimental versus predicted head pressure over time on the left side and overflow on the right side, using the *modInlet* setup. Numerical results are additionally corrected to exclude estimated static error.

The increase in flow rate between 0.2 s and 0.28 s in the *modVolute* setup can be explained when looking at the system head pressure outlined in Figure 3.12. The system head pressure is calculated using the pressures in both reservoirs. Thereby, the 20 cm long outlet graft is included. Not only is additional inertia introduced by the fluid in the outlet graft visible due to the widening of the loop, but also the fact that the head pressure reaches zero. According to the characteristic equation 1.16, introduced in Section 1.3.2, a specific flow rate is expected at a head pressure

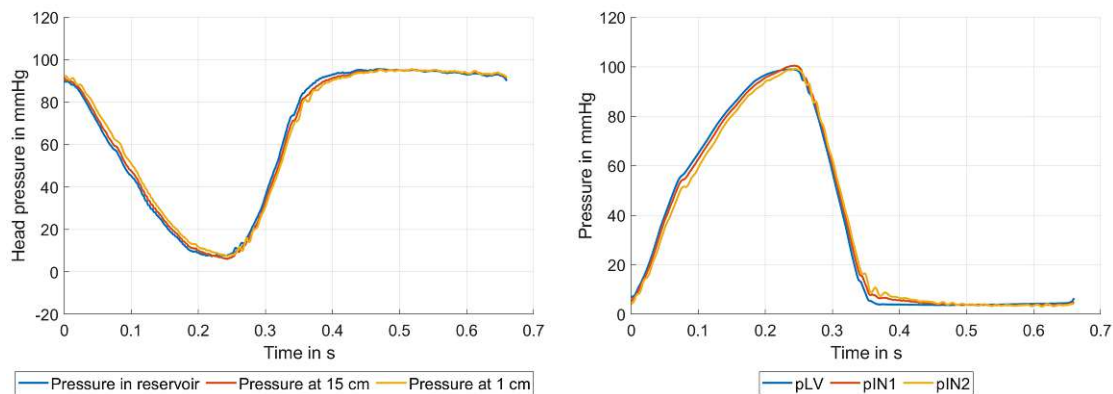


Figure 3.11: Head pressures calculated with the pressure sensor in the reservoir, 15 cm and 1 cm in front of the cannula and the same outlet pressure are illustrated on the left side, and the corresponding pressures themselves are depicted on the right side.

of zero and a certain impeller speed.

An increase in flow rate at constant head pressure could be possible if either the pump suddenly operates more efficiently or the speed of the impeller is increased. The measured speed of the impeller, see Figure 3.3, does not show an increase; therefore, this cause can be discarded. While the effect of impeller displacement has been statically discarded, detecting possible eddies that influence the hydraulic efficiency of the pump is not possible with the current experimental setup. The numerical prediction of such eddies requires a precise understanding of the trajectory of the impeller, which is currently under investigation.

Another explanation could be an incorrect measurement. Although it has been statically proven that the pressure at the top of the reservoir correctly reflects the pressure upstream of the cannula, this does not necessarily apply to the dynamic application or operation points with higher flow rates. A higher pressure in front of the cannula than measured would result in a lower pressure head and, therefore, a higher mass flow. The comparison of the pressures measured in the *modInlet* setup provides a further indication. As shown in Figure 3.11, the pressure *pIN1*, measured 5 cm downstream of the reservoir, has no plateau and exceeds the reservoir pressure.

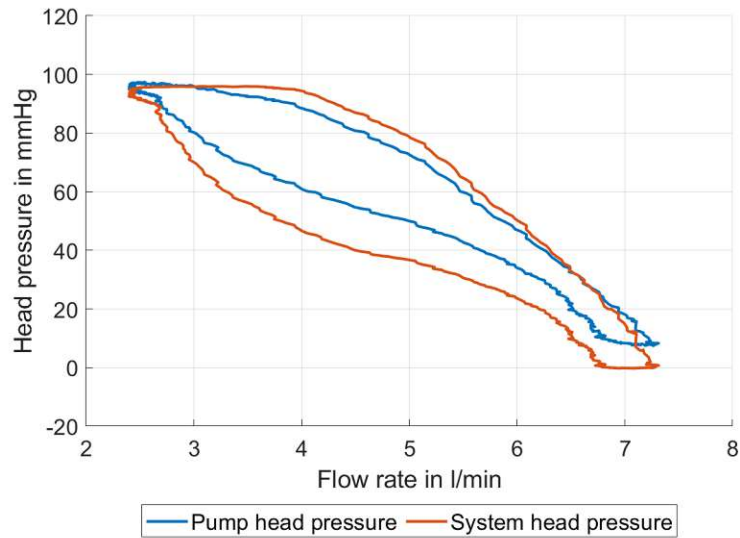


Figure 3.12: Dynamic characteristic loop of the pump itself using the pressure sensor placed at the pump outlet and of the system, including the outlet graft using the pressure sensor in the aortic reservoir.

3.3.2 Numerical Results

In contrast to the static investigation done at 4.5 L/min, it is reasonable to model turbulence as differences are clearly visible. Thamsen et al. compared different turbulence models and suggested the *Reynolds stress model*.

While the *moving reference frame* method in combination with *mixing plane* averaging, especially with the option to use large time steps, provides an inexpensive prediction of global performance, the use of the *frozen rotor* method is not working. For detailed local flow investigations, *sliding mesh* with time steps below 16 degrees is recommended to resolve the pressure fluctuations.

For the prediction of the head pressure and the global performance of the LVAD, the reference pressure can be set at either the inlet or outlet. When investigating local flow phenomena, setting the reference pressure at the inlet and the mass flow as a time-varying boundary condition at the outlet is advised. With this setup, the fluctuation in pressure due to bypassing the impeller blades is predicted plausibly. The use of two time-varying pressure boundary conditions has not been investigated since this would require distant boundaries not to constrain the pressure, which is

impossible as the pump is mounted in the reservoir.

Since the impeller is driven electromagnetically, the speed is not constant but fluctuates less than 1.2%. It has been shown that this fluctuation can be neglected.

3.3.3 Comparison of Experimental and Numerical Results

To validate the simulation, the *modInlet* setup is used since the increase in the flow rate is not reproduced by the numerical setup. Although the comparison with the *modInlet* setup is sufficient to validate the simulation, it does not correspond to the physiological application, as the LVAD entrains the flow directly from the left ventricle.

Since the experimental head in systole and the predicted head in diastole are on a wider trajectory, the deviation cannot be explained by a different inertia constant. The largest deviation appears to be in the middle range of the flow rate and flattens out towards the minimum and maximum flow rate values. This indicates that the observed error may be of second order.

The end-diastolic and end-systolic head pressures are part of the characteristic curve and, therefore, can be considered as static operation points. With the static operation point investigated in Chapter 2, three static operation points and their deviation compared with the experiment are known. The static error of each point and a fitted polynomial of second order are outlined in Figure 3.13 on the left side.

If the dynamically predicted head pressure is corrected with the fitted polynomial representing the static error, the corrected predicted head pressure agrees with the experimental results (absolute RMSE: 2.28 *mmHg*, relative RMSE: 1.027, ratio of enclosed area: 0.85) as illustrated in Figure 3.13 on the right side. Therefore, the simulation setup can predict the dynamic behaviour correctly. Furthermore, the deviation is due to a false prediction of the static head pressure.

3.4 Conclusion

One of the primary challenges in developing a rotodynamic blood pump is ensuring its safe operation. Therefore, CFD is commonly employed to predict blood damage. Dynamic simulations are required to replicate the physiological conditions

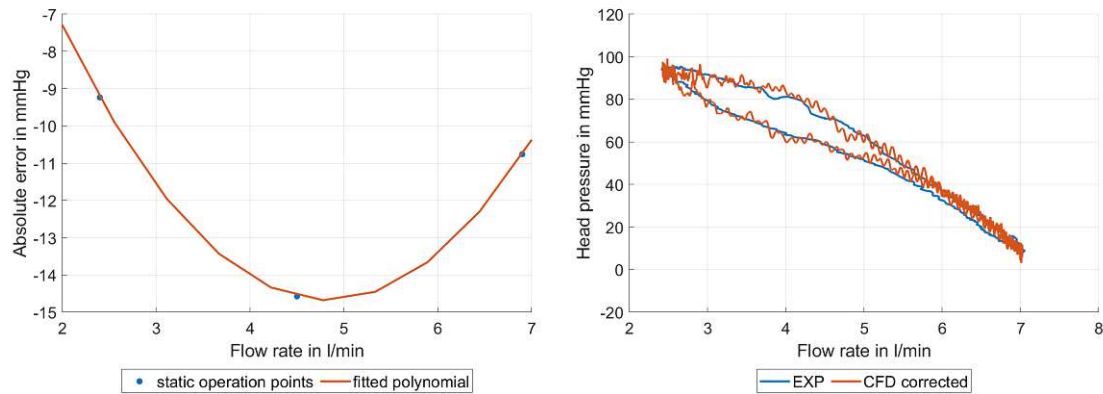


Figure 3.13: Absolute error of static operation points and fitted polynomial of second order is shown on the left. The corrected dynamic characteristic agrees with the experimental results.

accurately.

This study demonstrated that dynamic characteristics influenced by inertia effects can be precisely predicted when static deviations are corrected. Consequently, investigating dynamic characteristics requires validated or corrected static simulations that cover the entire flow rate range.

Furthermore, several insights were obtained regarding the simulation setup. Modelling turbulence is advisable for simulating higher flow rates, including dynamic applications. When investigating global parameters such as head pressure, using the *moving reference frame* method combined with *mixing plane* averaging is effective. In contrast, the *frozen rotor* approach fails to predict head pressure accurately. Additionally, the *mixing plane* averaging method allows for significantly larger time steps when predicting global performance, thereby reducing computational costs. Boundary conditions involving time-varying mass flow and reference pressure were effective in both configurations, although setting the outlet mass flow is physically more plausible. No influence of impeller speed fluctuations was observed.

Bibliography

- [1] Alfonsi, G. (2009). Reynolds-Averaged Navier–Stokes Equations for Turbulence Modeling. *Applied Mechanics Reviews* 62, DOI: [10.1115/1.3124648](https://doi.org/10.1115/1.3124648).
- [2] Bender, M., Escher, A., Messner, B., Röhrich, M., Fischer, M. B., Hametner, C., Laufer, G., Kertzsch, U., Zimpfer, D., Jakubek, S., and Granegger, M. (2024). An Atraumatic Mock Loop for Realistic Hemocompatibility Assessment of Blood Pumps. *IEEE Transactions on Biomedical Engineering* 71, 1651–1662.
- [3] Boes, S., Thamsen, B., Haas, M., Daners, M. S., Meboldt, M., and Granegger, M. (2019). Hydraulic Characterization of Implantable Rotary Blood Pumps. *IEEE Transactions on Biomedical Engineering* 66, 1618–1627.
- [4] Bourque, K., Cotter, C., Dague, C., Harjes, D., Dur, O., Duhamel, J., Spink, K., Walsh, K., and Burke, E. (2016). Design Rationale and Preclinical Evaluation of the HeartMate 3 Left Ventricular Assist System for Hemocompatibility. *ASAIO Journal* 62, 375–383.
- [5] Brooks, D. E., Goodwin, J. W., and Seaman, G. V. (1970). Interactions among erythrocytes under shear. *Journal of Applied Physiology* 28, 172–177.
- [6] Celik, I. B., Ghia, U., Roache, P. J., Freitas, C. J., Coleman, H., and Raad, P. E. (2008). Procedure for Estimation and Reporting of Uncertainty Due to Discretization in CFD Applications. *Journal of Fluids Engineering* 130, DOI: [10.1115/1.2960953](https://doi.org/10.1115/1.2960953).
- [7] Chen, Z., Jena, S. K., Giridharan, G. A., Koenig, S. C., Slaughter, M. S., Griffith, B. P., and Wu, Z. J. (2018). Flow features and device-induced blood trauma in CF-VADs under a pulsatile blood flow condition: A CFD comparative study. *International Journal for Numerical Methods in Biomedical Engineering* 34, e2924.
- [8] Chien, K.-Y. (1982). Predictions of Channel and Boundary-Layer Flows with a Low-Reynolds-Number Turbulence Model. *AIAA Journal* 20, 33–38.
- [9] Eisen, H. J. (2019). Left Ventricular Assist Devices (LVADS): History, Clinical Application and Complications. *Korean Circulation Journal* 49, 568.

- [10] Escher, A., Hubmann, E. J., Karner, B., Messner, B., Laufer, G., Kertzsch, U., Zimpfer, D., and Granegger, M. (2022). Linking Hydraulic Properties to Hemolytic Performance of Rotodynamic Blood Pumps. *Advanced Theory and Simulations* 5, 2200117.
- [11] Escher, A., Thamsen, B., Strauch, C., Kertzsch, U., Zimpfer, D., Thamsen, P. U., and Granegger, M. (2023). In-Vitro Flow Validation of Third-Generation Ventricular Assist Devices: Feasibility and Challenges. *ASAIO Journal* 69, 932–941.
- [12] Eurotransplant - Statistics.
- [13] Garcia Villalba Navaridas, M. Fundamentals of numerical thermo-fluid dynamics, 2023.
- [14] Giersiepen, M., Wurzing, L. J., Opitz, R., and Reul, H. (1990). Estimation of shear stress-related blood damage in heart valve prostheses—in vitro comparison of 25 aortic valves. *The International Journal of Artificial Organs* 13, 300–306.
- [15] Grinstein, J., Torii, R., Bourantas, C. V., and Garcia-Garcia, H. M. (2021). Left Ventricular Assist Device Flow Pattern Analysis Using a Novel Model Incorporating Left Ventricular Pulsatility. *ASAIO Journal* 67, 724–732.
- [16] Gülich, J. F., *Centrifugal Pumps*; Springer Berlin Heidelberg: Berlin, Heidelberg, 2010.
- [17] Hahne, M., Crone, V., Thomas, I., Wolfgramm, C., Liedtke, F. K. P., Wurm, F.-H., and Torner, B. (2024). Interaction of a Ventricular Assist Device With Patient-Specific Cardiovascular Systems: In-Silico Study With Bidirectional Coupling. *ASAIO Journal*, DOI: [10.1097/MAT.0000000000002181](https://doi.org/10.1097/MAT.0000000000002181).
- [18] HEARTMATE 3™ LEFT VENTRICULAR ASSIST SYSTEM - Instruction Of Use, 2018.
- [19] Huang, F., Lei, H., Ying, S., Fu, Y., Li, Q., and Ruan, X. (2023). Numerical hemolysis performance evaluation of a rotary blood pump under different speed modulation profiles. *Frontiers in Physiology* 14, 1116266.
- [20] Issa, R. I. (1986). Solution of the implicitly discretised fluid flow equations by operator-splitting. *Journal of Computational Physics* 62, 40–65.
- [21] Kok, J. C. (2000). Resolving the dependence on freestream values for the k-omega turbulence model. *AIAA Journal* 38, 1292–1295.

- [22] Kurtyka, P., Kustos, R., Kaczmarek, M., Gonsior, M., and Tokarska, K. Surface modifications for inflow cannulas of ventricular assist devices – comparison of latest solutions. *Engineering of Biomaterials 2019*, 17–23.
- [23] Lee, L. S., and Shekar, P. S. (2014). Current state-of-the-art of device therapy for advanced heart failure. *Croatian Medical Journal 55*, 577–586.
- [24] Levine, A., and Gass, A. (2019). Third-Generation LVADs: Has Anything Changed? *Cardiology in Review 27*, 293–301.
- [25] Li, H., Gou, Z., Huang, F., Ruan, X.-d., Qian, W.-w., and Fu, X. (2019). Evaluation of the hemolysis and fluid dynamics of a ventricular assist device under the pulsatile flow condition. *Journal of Hydrodynamics 31*, 965–975.
- [26] Li, S., Jin, D., and Gui, X. (2023). Dynamic characteristic modeling of left ventricular assist devices based on hysteresis effects. *Computers in Biology and Medicine 157*, 106737.
- [27] Linneweber, J., Dohmen, P. M., Kerzschner, U., Affeld, K., Nosé, Y., and Konertz, W. (2007). The Effect of Surface Roughness on Activation of the Coagulation System and Platelet Adhesion in Rotary Blood Pumps. *Artificial Organs 31*, 345–351.
- [28] Maltais, S., Kilic, A., Nathan, S., Keebler, M., Emani, S., Ransom, J., Katz, J. N., Sheridan, B., Brieke, A., Egnaczyk, G., Entwistle, J. W., Adamson, R., Stulak, J., Uriel, N., O’Connell, J. B., Farrar, D. J., Sundareswaran, K. S., and Gregoric, I. (2017). PREVENTion of HeartMate II Pump Thrombosis Through Clinical Management: The PREVENT multi-center study. *The Journal of Heart and Lung Transplantation 36*, 1–12.
- [29] Mansour, N. N., Kim, J., and Moin, P. (1989). Near-wall k-epsilon turbulence modeling. *AIAA Journal 27*, 1068–1073.
- [30] Mehra, M. R., Naka, Y., Uriel, N., Goldstein, D. J., Cleveland, J. C., Colombo, P. C., Walsh, M. N., Milano, C. A., Patel, C. B., Jorde, U. P., Pagani, F. D., Aaronson, K. D., Dean, D. A., McCants, K., Itoh, A., Ewald, G. A., Horstman-shof, D., Long, J. W., and Salerno, C. (2017). A Fully Magnetically Levitated Circulatory Pump for Advanced Heart Failure. *New England Journal of Medicine 376*, 440–450.
- [31] Mehra, M. R. et al. (2019). A Fully Magnetically Levitated Left Ventricular Assist Device — Final Report. *New England Journal of Medicine 380*, 1618–1627.

- [32] Menter, F. R. (1994). Two-equation eddy-viscosity turbulence models for engineering applications. *AIAA Journal* 32, 1598–1605.
- [33] Milano, C. A., Rogers, J. G., Tatooles, A. J., Bhat, G., Slaughter, M. S., Birks, E. J., Mokadam, N. A., Mahr, C., Miller, J. S., Markham, D. W., Jeevanandam, V., Uriel, N., Aaronson, K. D., Vassiliades, T. A., and Pagani, F. D. (2018). HVAD: The ENDURANCE Supplemental Trial. *JACC: Heart Failure* 6, 792–802.
- [34] Moazami, N., Fukamachi, K., Kobayashi, M., Smedira, N. G., Hoercher, K. J., Massiello, A., Lee, S., Horvath, D. J., and Starling, R. C. (2013). Axial and centrifugal continuous-flow rotary pumps: A translation from pump mechanics to clinical practice. *The Journal of Heart and Lung Transplantation* 32, 1–11.
- [35] Noor, M. R., Ho, C. H., Parker, K. H., Simon, A. R., Banner, N. R., and Bowles, C. T. (2016). Investigation of the Characteristics of HeartWare HVAD and Thoratec HeartMate II Under Steady and Pulsatile Flow Conditions. *Artificial Organs* 40, 549–560.
- [36] Numan, L., Schramm, R., Oerlemans, M. I., Van Der Kaaij, N. P., Aarts, E., Ramjankhan, F. Z., Oppelaar, A.-M., Morshuis, M., Guenther, S. P., Zimpfer, D., Riebandt, J., Wiedemann, D., Asselbergs, F. W., and Van Laake, L. W. (2023). Survival after HeartMate 3 left ventricular assist device implantation: real-world data from Europe. *ESC Heart Failure* 10, 2754–2756.
- [37] Pae, W. E., and Lundblad, O. (1999). Thoratec Paracorporeal Pneumatic Ventricular Assist Device. *Operative Techniques in Thoracic and Cardiovascular Surgery* 4, 352–368.
- [38] Pollock, J. D., and Makaryus, A. N., Physiology, Cardiac Cycle In *StatPearls [Internet]*; StatPearls Publishing: 2022.
- [39] Ponikowski, P. et al. (2016). 2016 ESC Guidelines for the diagnosis and treatment of acute and chronic heart failure: The Task Force for the diagnosis and treatment of acute and chronic heart failure of the European Society of Cardiology (ESC) Developed with the special contribution of the Heart Failure Association (HFA) of the ESC. *European Heart Journal* 37, 2129–2200.
- [40] Reichardt, H. (1951). Vollständige Darstellung der turbulenten Geschwindigkeitsverteilung in glatten Leitungen. *ZAMM - Journal of Applied Mathematics and Mechanics / Zeitschrift für Angewandte Mathematik und Mechanik* 31, 208–219.

- [41] Rogers, J. G., Pagani, F. D., Tatooles, A. J., Bhat, G., Slaughter, M. S., Birks, E. J., Boyce, S. W., Najjar, S. S., Jeevanandam, V., Anderson, A. S., Gregoric, I. D., Mallidi, H., Leadley, K., Aaronson, K. D., Frazier, O., and Milano, C. A. (2017). Intrapericardial Left Ventricular Assist Device for Advanced Heart Failure. *New England Journal of Medicine* 376, 451–460.
- [42] Rose, E. A., Stevenson, L. W., and Tierney, A. R. (2001). Long-Term Use of a Left Ventricular Assist Device for End-Stage Heart Failure. *The New England Journal of Medicine*.
- [43] Secomb, T. W. (2016). Hemodynamics. *Comprehensive Physiology* 6, 975–1003.
- [44] Slaughter, M. S., Rogers, J. G., Milano, C. A., Russell, S. D., Conte, J. V., Feldman, D., Sun, B., Tatooles, A. J., Delgado, R. M., Long, J. W., Wozniak, T. C., Ghumman, W., Farrar, D. J., and Frazier, O. H. (2009). Advanced Heart Failure Treated with Continuous-Flow Left Ventricular Assist Device. *New England Journal of Medicine* 361, 2241–2251.
- [45] Software, S. D. I. Simcenter STAR-CCM+ User Guide 2210, 2022.
- [46] Song, X., Throckmorton, A. L., Wood, H. G., Allaire, P. E., and Olsen, D. B. (2004). Transient and Quasi-Steady Computational Fluid Dynamics Study of a Left Ventricular Assist Device. *ASAIO Journal* 50, 410–417.
- [47] Spalart, P., and Allmaras, S. (1992). A One-Equation Turbulence Model for Aerodynamic Flows. *AIAA* 439, DOI: [10.2514/6.1992-439](https://doi.org/10.2514/6.1992-439).
- [48] Stepanoff, A. J., *Centrifugal and Axial Flow Pumps*, 2nd, 1948.
- [49] Strüber, M., Meyer, A. L., Malehsa, D., Kugler, C., Simon, A. R., and Haverich, A. (2009). The Current Status of Heart Transplantation and the Development of „Artificial Heart Systems“. *Deutsches Ärzteblatt international*, DOI: [10.3238/arztebl.2009.0471](https://doi.org/10.3238/arztebl.2009.0471).
- [50] Thamsen, B., Gülan, U., Wiegmann, L., Loosli, C., Schmid Daners, M., Kurtcuoglu, V., Holzner, M., and Meboldt, M. (2020). Assessment of the Flow Field in the HeartMate 3 Using Three-Dimensional Particle Tracking Velocimetry and Comparison to Computational Fluid Dynamics. *ASAIO Journal* 66, 173–182.

- [51] Torner, B., Duong, D. V., and Wurm, F.-H. (2023). Numerical Determination of the Equivalent Sand Roughness of a Turbopump's Surface and Its Roughness Influence on the Pump Characteristics. *International Journal of Turbomachinery, Propulsion and Power* 8, 5.
- [52] Tsukamoto, H., and Ohashi, H. (1982). Transient Characteristics of a Centrifugal Pump During Starting Period. *Journal of Fluids Engineering* 104, 6–13.
- [53] Wang, V.-H., Li, K.-H., and Li, J.-Y. (2021). The influence of wall roughness on centrifugal pump performance. *IOP Conference Series: Materials Science and Engineering* 1081, 012054.
- [54] Wiegmann, L., Thamsen, B., De Zélicourt, D., Granegger, M., Boës, S., Schmid Daners, M., Meboldt, M., and Kurtcuoglu, V. (2019). Fluid Dynamics in the HeartMate 3: Influence of the Artificial Pulse Feature and Residual Cardiac Pulsation. *Artificial Organs* 43, 363–376.
- [55] Wilcox, D. C. (1988). Reassessment of the scale-determining equation for advanced turbulence models. *AIAA Journal* 26, 1299–1310.
- [56] Yamada, Y., Nishinaka, T., Mizuno, T., Taenaka, Y., Tatsumi, E., and Yamazaki, K. (2011). Neointima-inducing inflow cannula with titanium mesh for left ventricular assist device. *Journal of artificial organs* 14, 269–275.